

Note: This is a preprint and is not peer-reviewed.

This research has been submitted to “Frontiers in Climate”

Quantifying potential carbon dioxide removal via enhanced weathering using porewater from a field trial in Scotland

Amy L McBride^{1*}, Kirstine Skov^{2*}, Peter Wade², Joey Betz^{2,3}, Amanda Stubbs², Tzara Bierowiec², Talal Albahri², Giulia Cazzagon², Chieh-Jhen Chen², Amy Frew², Matthew Healey², Ifeoma Idam⁴, Lucy Jones², Mike E Kelland⁵, Jim Mann², David Manning⁶, Callum Mitchell², Melissa J Murphy⁷, Anežka Radkova⁹, Marta-Villa de toro Sanchez⁸, Utku Solpuker¹⁰, Yit Arn Teh⁵, Rosalie Tostevin², Will Turner², Jez Wardman¹¹, Morven Wilkie², XinRan Liu².

¹Independent Researcher, Freiburg-im-Breisgau, Germany

²UNDO Carbon Ltd., London, United Kingdom

³Department of Physics, University College London, London, United Kingdom

⁴Keel, Long Hanborough, United Kingdom

⁵Weathering Industries Ltd, Sheffield, United Kingdom

⁶School of Natural and Environmental Sciences, Newcastle University, Newcastle upon Tyne, Tyne and Wear, United Kingdom

⁷Mel Murphy Geochemistry, Copenhagen, Denmark

⁸Institute of Earth Sciences, University of Lausanne, Switzerland

⁹Independent Researcher, Cambridge, United Kingdom

¹⁰Independent Researcher, Lyon, France

¹¹Independent Agronomist, Angus, Scotland

* **Correspondence:**

almcbride143@gmail.com

kirstine.skov@un-do.com

Keywords: Enhanced weathering, MRV, porewater, CDR, field trial.

Abstract

Enhanced weathering (EW) is cited as a promising carbon dioxide removal (CDR) strategy, and is being rapidly commercialized. Rigorous monitoring, reporting and verification (MRV) are essential to ensure carbon claims are accurate and carbon credits are not mis-sold. MRV protocols incorporate multiple approaches, including soil and porewater sampling. This paper calculates potential CDR from porewater, via an alkalinity estimation calculated from charge balance, and from soil samples, via the accumulation of exchangeable cations on soil exchange sites. These potential CDR estimations are then compared to the maximum theoretical CDR potential. The data were collected from a 1.5 year field trial, situated in south-east Scotland. Crushed basalt was surface-applied to plots at rates of 0 (control), 23, 78 and 126 t ha⁻¹. To calculate direct-measured potential CDR (direct pCDR) from porewater, ion concentrations of porewater samples extracted from a depth of 5 and 10 cm were integrated with precipitation surplus to estimate the flux of cations leaching from each depth over *c.* two week periods, as water budgets allowed. Generalized linear model results identified a significant effect of treatment as an explanatory variable for potential CDR, both at 5 and 10 cm depth. Significant potential CO₂ removal ranging from 0.33 to 0.53 tCO₂ ha⁻¹ after *c.* 1.5 years of weathering was calculated in the 5 cm depth treatment in the 78 and 126 t ha⁻¹ application treatment relative to the control. No significant difference was observed between the control and the 23 t ha⁻¹ treatment at 5 cm depth, nor were there any significant differences in the 10 cm treatments when evaluated relative to the control. Carbonate precipitation was also assessed, but remained below the detection limit. Potential CDR (inferred pCDR) calculated from the exchangeable cation pool (ammonium acetate extractable pool) in 30 cm-deep soil samples revealed no significant inferred pCDR, possibly as a result of experimental design and sampling density. Overall, when direct pCDR is normalized to mass of rock applied and duration of weathering (e.g. mass-time-normalized-pCDR), the values fall within the mid-range of values published from other field studies.

1 Introduction

Gigaton-scale durable carbon dioxide removal (CDR) is required, alongside rapid reductions in greenhouse gas emissions, in all scenarios that limit warming to 1.5°C above pre-industrial temperatures (Mignone et al., 2024). Currently, conventional CDR (e.g. afforestation and wetland restoration) removes 2.1 GtCO₂ yr⁻¹, but by 2050, a CDR scale-up of *c.* 7.2 GtCO₂ yr⁻¹ is required to meet these targets (Smith et al., 2024). ‘Novel’ CDR (e.g. biochar, bioenergy with carbon capture and storage and enhanced weathering (EW)) is expected to account for *c.* 3.4 GtCO₂ yr⁻¹ of this additional CDR by 2050, but currently, contributes only 0.0013% to global CDR efforts (Smith et al., 2024). When comparing CDR pathways, durability is an important consideration, to prevent re-release of CO₂, with research showing that durability extending beyond 1,000-years is required to stabilize global temperatures (Brunner et al., 2024).

One promising novel CDR technology is EW, which aims to accelerate the weathering of silicate (and carbonate) minerals – a natural CDR process that already removes

c. 1 Gt CO₂ yr⁻¹ globally (Berner and Berner, 2012). This weathering mechanism involves silicate minerals dissolving into solution by hydrolysis, where water attacks the metal silicates in acidic, neutral or basic environments. The process releases base cations (Ca²⁺, Mg²⁺, Na⁺ and K⁺) into solution with concomitant production of hydroxide ions. The carbon capture mechanism involves the natural dissolution of CO₂ produced via soil respiration into water, forming carbonic acid (H₂CO₃). The reaction of the carbonic acid with the hydroxide ions converts the carbonic acid (ex CO₂(atm)) into dissolved bicarbonate (HCO₃⁻). In this way, base cations released from the rock (via rock weathering) are charge balanced by bicarbonate (removing carbon from the atmosphere) during transport to the ocean through hydrological and natural geochemical systems, where the transformed carbon can remain stable for *c.* 100,000 years (Renforth and Henderson, 2017). Part of the transformed carbon (currently *c.* 13%) is re-released once reaching the ocean due to ocean carbonate buffering (Renforth and Henderson, 2017). Where substantial inorganic carbon, Ca²⁺ and high pH (typically > 8.5) are present, carbonate minerals may also precipitate in soils, and sequester carbon in a solid phase instead (Jorat et al., 2022). During the precipitation of carbonate, the efficacy of CDR is halved, to one mole of carbon per mole of divalent cation.

Rocks containing relatively high concentrations of Mg²⁺ and Ca²⁺, such as mafic and ultramafic rocks (*c.* 8-54 wt.% CaO + MgO (Renforth, 2012)) are more favorable for EW due to their higher CDR potential (Renforth, 2012) and faster dissolution kinetics (Wolff-Boenisch et al., 2006; Heřmanská et al., 2022). Several methods have been proposed to accelerate natural rock weathering (Hartmann et al., 2013). One such method involves the application of crushed Ca- and Mg-rich silicate rocks onto croplands (e.g. Beerling et al., 2018, 2020; Kantola et al., 2017). Rock weathering is accelerated because of (1) increased surface area of crushed rock (either freshly crushed or available as a by-product, whereby no carbon penalty for crushing is required) relative to outcrop, (2) distribution of crushed rock into soils, which can increase their wetted reactive surface area, reduce dissolution-limiting saturation effects and thus increase their weathering rate and (3) increased *p*CO₂ concentrations - which are between 3-to-10-fold higher in soils compared to atmospheric concentrations (Nan et al., 2016; Dietzen and Rosing, 2023).

There are four key reasons why EW in agricultural soils is considered a highly promising CDR pathway: (1) utilization of existing land, (2) resource abundance, (3) compatibility with existing technologies, and (4) agronomic co-benefits. Firstly, nearly 11%

of the Earth's surface is dedicated to agriculture, so there is minimal land use change required to deploy EW (Beerling et al., 2018). Secondly, there is an abundance of suitable crushed rock, with over 3 billion tons produced annually (Renforth et al., 2011). Mafic rocks also comprise *c.*5.2% of Earth's land surface (Amiotte Suchet et al., 2003), forming large reserves of uncrushed rocks that could be mined as necessary. Thirdly, the infrastructure and technology required to facilitate the spreading of crushed rock already exists from the liming and fertilizer industry, obviating the need for further technological development (Beerling et al., 2018). Finally, EW does not compete with land used for food production, and instead, has the potential to boost soil pH and crop yields (e.g. Beerling et al., 2024; Skov et al., 2024). The latter incentivizes the application of crushed silicate rocks to farmers whose land could be used for enhanced weathering operations.

These four reasons contribute to the attractiveness of EW as a CDR technology. Model simulations which integrate proxies for rock weathering, as well as land, climate and infrastructure data, have shown that EW could contribute substantially (between 0.5 and 2 Gt CO₂ yr⁻¹) to global CDR targets (Beerling et al., 2020). As a result of these predictions and other modelling studies (Kelland et al., 2020; Lewis et al., 2021; Kantzas et al., 2022), as well as experimental data (Haque et al., 2020; Kelland et al., 2020; Amann et al., 2022; Larkin et al., 2022; McDermott et al., 2024), over 20 start-ups focused on EW have been founded (CDR.fyi, 2025). Many of these companies conduct rock-spreading operations and have raised over \$46 million USD in equity investment (CDR.fyi via personal communication).

While EW has a high potential, there are several challenges associated with proving that CDR via EW has occurred. These challenges arise from: (1) operating in an open system where the removed carbon is stored in a different location (i.e. the marine environment) from where it was initially removed from the atmosphere (i.e. agricultural soils), (2) complexity associated with biogeochemical processes from source to sink (e.g. degassing downstream, seasonal carbonate precipitation) and (3) difficulty resolving small signals against high background variability (Schulte et al., 2024). Despite these challenges, it remains imperative that robust Monitoring, Reporting and Verification (MRV) of EW is in place to ensure the credibility of carbon credits sold and build trust in the CDR market (Smith et al., 2024).

The theoretical maximum CDR potential of a given rock can be estimated based on analyses of concentrations of base cation oxides (CaO, MgO, Na₂O, K₂O) and non-metal oxides (SO₃, P₂O₅) of feedstocks (Renforth, 2012, 2019). However, these estimates currently

bear no relation to field weathering rates and can thus only be used for feedstock comparisons. For durable CDR via EW to occur, bicarbonate charge balanced by base cations must either be: (1) in transit to ocean storage or (2) precipitated as inorganic carbon in soils. To measure the transit of samples to the ocean, liquid samples are required to be analyzed for both base cations and anions to estimate bicarbonate. Bicarbonate can also be determined through the measurement of two of: pH, alkalinity, or dissolved inorganic carbon (Buss and Hasemer, 2024). Soil samples can be tested to identify precipitated inorganic carbon in soils, though seasonal precipitation/redissolution may occur (e.g. Jorat et al., 2022).

Indeed, the most recent methodologies published by crediting registries require that the CDR via increased bicarbonate flux is quantified from either: (1) soil porewater taken at shallow depths below the near field zone (NFZ) (i.e the zone where weathering processes directly affect atmospheric CO₂ concentrations) or (2) determined via a mass balance approach where CDR is assumed to be the balance between rock weathering and all other sinks for cations in an agricultural environment within the NFZ: plant uptake, storage on soil cation exchange sites, carbonate precipitation and strong acid weathering (Sutherland et al., 2024). Both methods are labor intensive and require large numbers of analytical samples. In the future, once large datasets have been collated, it may be possible to reduce the number of measurements (and thus cost of EW MRV) through simplified sample measurements or geochemical modelling.

A wealth of meso-scale experimental data exists, but fewer EW field trials have had their results published to this date (McDermott et al., 2024). Field trials have quantified CDR via EW using: (1) soil leachate or porewater sampling (Deng et al., 2024; McDermott et al., 2024), (2) riverine sampling (Taylor et al., 2021; Larkin et al., 2022), (3) soil mass balance approaches (e.g. Beerling et al., 2024; Dietzen & Rosing, 2023) and (4) via carbonate precipitation (Haque et al., 2020). Riverine sampling allows the direct quantification of CDR. However, it is challenging to identify suitable control and treatment catchments along agricultural fields which are required to identify additional bicarbonate fluxes (CDR), though identifying suitable catchments along agricultural fields may be challenging as it is challenging to identify control catchments to subtract additional bicarbonate fluxes from, thus CDR. Soil mass balance approaches integrated with additional sinks infer CDR while bicarbonate that is either measured or calculated using porewater collected from the boundary

of or beyond the near field zone is a more direct measure of CDR at that point in space and time.

Hydrological information is required to convert porewater concentration data into a flux of CDR. Leachate volumes can be quantified in mesoscale experiments because leachate is directly collected into a separate vessel. Implementing leachate collection vessels in fields to record leachate weight is costly. Therefore, several studies have used monthly or annual climatic data to assume water flux (McDermott et al., 2024). Annual data may, however, exaggerate fluxes in drier, hotter months and underestimate contributions in wetter, colder months (e.g. Warken et al., 2024).

This paper compares several methods described for calculating CDR using a 1.5 year long porewater time series as well as soil samples taken from a 28-month period from an EW field trial located in Scotland, UK. Data from two potential CDR calculation methods, using (1) soil porewater chemistry from 5 and 10 cm (collected *c.* 2-weekly porewater) integrated with daily precipitation surplus data and (2) exchangeable cations from 0-30 cm depth. These data are compared with the maximum theoretical CDR determinations using the E_{pot} equation (Renforth et al., 2019) to gain an insight into the differences in CDR estimations. Both methods are referred to as ‘potential CDR’ because: (1) porewater was not sampled below the NFZ and (2) the accumulation of cations on exchange sites (ExPot) are not currently charge balancing bicarbonates. However, pCDR calculated from porewater is referred to as ‘direct pCDR’ and ExPot is referred to as ‘inferred pCDR’.

2. Methods

2.1. Field location and experimental design

The field site is located on The Future Forest Company-managed Estate, Dumyat, near Stirling, Scotland (56.14930789 N; -3.89292692 W), and is referred to as Dumyat throughout this paper (Figure 1). The site is a grassland pasture, which is periodically used for grazing cattle and sheep from late summer to early autumn. The site is situated on a flat area of land at the bottom of a hillslope (field site gradient = 2°). The site is underlain with historic drainpipes running in the North-South direction. During the field trial, no fertilizer was applied to the field site.

The climate of the site is characterized as temperate oceanic, according to the Köppen-Geiger classification scheme (Beck et al., 2018). Directly before the experiment began, the 10-year average annual temperature was 10.1°C and the average daily precipitation-evapotranspiration (P-ET) was 1.6 mm. During the course of the experiment, the average daily P-ET was 2.8 mm and annual average temperature was 8.2°C. The seasonality in the observed P-ET over the duration of the experiment can be found in Figure 2.

Four experimental plots, each 48 x 100 m in size were set up in September 2022. Between the plots a buffer of 12 m was established, corresponding to the width of one pass with the agricultural lime spreader that was used for basalt deployment. Each plot was amended to a different basalt application rate (0, 23, 78 and 126 tons ha⁻¹, see Figure 1). Within each plot a central area was established, and three sets of soil porewater macro-rhizon samplers (pore size of the membrane 0.12 - 0.18 µm) were installed to the North, East and West of this central point via soil pits at 5 and 10 cm depth. The soil pits in which the rhizons were placed were 3 m from a central point, with straight-line distances of 5.2 m between the pits. The rhizons were fenced off using wooden fencing to prevent equipment damage from livestock and wildlife.

The basalt application was surface-applied in two stages. The majority of the plot was spread using a commercial lime spreader on the 20th September 2022. The central fenced off area was spread using a hand sieve on the 27th September 2022 to ensure an even spreading distribution across the area where porewater extraction was conducted.

2.2. Soil baseline results

Baseline soil samples were collected on the 19th September 2022 (1 day before basalt spreading) using an Eijkelkamp 'Edelman' auger ($\varnothing = 4$ cm) and a sample depth of 30 cm. Soil samples were taken in the larger plots where basalt was spread using a commercial spreader at the locations indicated in Figure 1. The soil samples were taken in a W-pattern across each plot and georeferenced using a Trimble dGPS. Larger soil clumps were removed with a cloth between sampling events if needed. Before each sample the auger flight was prepared by taking a disposable sample directly adjacent to the sample point, to avoid contamination between samples. Samples were collected using plastic bags. The sampling depth was

measured with a ruler until 30 cm depth was reached. Once collected, all samples were dried at $< 40^{\circ}\text{C}$, sieved to < 2 mm and stored in plastic containers until analysis.

Both baseline and monitoring soil samples were sent for analysis to the United Kingdom Accreditation Service (UKAS) tested and ISO accredited (ISO/IEC 17025:2017) lab NRM - part of Cawood Scientific Limited. Baseline soil samples were analyzed for soil texture, cation exchange capacity and major exchangeable cations, soil inorganic and organic carbon. Soil pH was determined in UNDO's in-house lab and bulk density measurements were determined at the UK Biochar Research Centre (University of Edinburgh). The analysis methods are described in Supplementary Material S4. Analysis of the baseline soil samples showed a very uniform soil texture across the entire field, classified as a silty clay loam according to the USDA soil taxonomy. Mean and standard deviation for soil organic carbon content, and exchangeable calcium, magnesium, potassium and sodium, as well as soil pH and bulk density in three different depths are reported in Table 1. Baseline soil samples were also analyzed for soil inorganic carbon, but all samples were below detection (<0.2 wt.%). Differences in baseline variables across the four plots were evaluated using an ANOVA. There were no differences between the four plots, except for exchangeable calcium and magnesium ($p < 0.05$). A Tukey's HSD post hoc test revealed that the significant differences were present between the control vs 23 t ha^{-1} , control vs 126 t ha^{-1} plots for calcium and control vs. 23 t ha^{-1} for magnesium. Model requirements of normality and homoscedasticity were tested using Shapiro-Wilk and White's Lagrange multiplier test, respectively. All variables met model requirements except exchangeable magnesium which showed slight heteroscedasticity ($p = 0.03$), indicating that differences should be considered cautiously. The statistical comparison was carried out using Python (version 3.9) and the package Statsmodels (version 0.14.4) (Seabold and Perktold, 2010).

2.3. Feedstock

For each of the treated fields, basalt from the Hillend quarry was applied. The quarry is situated in Airdrie, Ayrshire (55.88552 N; -3.88448 W) and is owned by Tillicoultry Quarries Ltd.

Eight kilograms of rock was taken from a quarry stockpile on the 10th August 2022. The mineralogy of the sample (using quantitative X-ray diffraction, XRD), chemistry (using X-ray fluorescence, XRF), particle size distribution (using laser diffraction analysis), and

specific surface area (SSA; using 5-point Brunauer-Emmett-Teller (BET) methodology N₂-adsorption analysis) were analyzed. Detailed methods for the mineralogical, chemical and SSA characterization referred to in this paper can be found in Skov et al. (2024, Appendix S2) and Supplementary Material S1 in this paper.

The samples contained 69.9% fast weathering minerals, when compared to mineral groupings from Lewis et al (2021) (Table 2). The crushed basalt had a surface area of BET SSA 0.917 m²g⁻¹, and the D₅₀ particle size was 1,006 μm. The particle size and whole-rock chemistry are described in the Supplementary Material (Figure S1 and Table S1 and S2, respectively).

2.4. Porewater extraction and measurement

The first porewater samples were collected from the rhizon samplers installed at the site on the 15th October 2022 (23 days after the basalt was applied to the fenced-off areas). Porewater samples were collected *c.* every two weeks (between 10-18 days) when soil saturation levels were sufficient for porewater extraction. Porewater was extracted using a vacuum that was set and left for 48 hours (for the first 170 days, until 7th March 2023) or 24 hours (for the last 410 days, from 21st March 2023 to 18th April 2024) to allow water to filter into a 30 mL plastic syringe.

After collection, the porewater samples were poured into clean, 50 mL polypropylene conical flasks and *c.* 3 mL of the solution was pipetted into a 15 mL falcon centrifuge tube and stored in a refrigerator before submission for Inductively Coupled Plasma Mass Spectrometry (ICP-MS) and ion chromatography (IC) analysis at Nottingham University. The ICP-MS and IC analysis methods can be found in Supplementary Material Section S2 and S3, respectively. pH was measured using an OMNIS Advanced Titrator with Magnetic Stirrer.

2.5. Soil monitoring sampling

Soil monitoring samples were collected from the same locations as the baseline soil samples, using dGPS to relocate the sampling points shown in Figure 1. The monitoring samples were analyzed for exchangeable cations, soil inorganic carbon, as well as soil pH, following the same procedure as for the baseline soil samples (Section 2.2 and Supplementary Material S4).

Baseline samples (Section 2.2) were taken the day before basalt application on the 19th September 2022. The following three monitoring samples were taken 4, 7 and 10 months after basalt application, whereas the last monitoring samples were taken in January 2025, one and half year after the previous monitoring sample and 28 months since the experiment began.

Additionally, on one singular sampling event, five composite samples each comprising 20 subsamples were taken in the control and 126 t ha⁻¹ plots. The samples were taken to a depth of 10 cm and subject to ammonium acetate extractions to calculate inferred pCDR from exchangeable cations only (Section 2.6.2) by Weathering Industries Ltd.

2.6. Calculations of CDR

2.6.1. Maximum theoretical CDR (E_{pot} equation)

The maximum theoretical CDR provides the maximum potential for CDR based on the oxide chemistry of the rock, given an infinite time window for weathering to occur (based entirely on thermodynamics and devoid of any consideration of kinetics). For this study, the maximum theoretical CDR was calculated using the E_{pot} equation (Renforth et al., 2019). The E_{pot} value provides a CDR estimate on a per unit weight basis (e.g. mass of CO₂ removed per mass of rock applied). This equation (Equation 1) considers the wt.% of various oxides (CaO, MgO, K₂O, Na₂O, P₂O₅ and SO₃) measured via XRF analysis (Table S1).

$$E_{pot} = \frac{M_{CO_2}}{100} \cdot \left(\alpha \frac{CaO}{M_{CaO}} + \beta \frac{MgO}{M_{MgO}} + \varepsilon \frac{Na_2O}{M_{Na_2O}} + \theta \frac{K_2O}{M_{K_2O}} + \gamma \frac{SO_3}{M_{SO_3}} \delta \frac{P_2O_5}{M_{P_2O_5}} \right) \cdot \omega \cdot AppD \quad (1)$$

Where: M_{CO_2} is the molar mass of CO₂ (44.01 g mole⁻¹), M(oxide) and %(oxide) are the molecular masses and wt.% of each of the oxides given in the equation. The coefficients α , β , ε , θ , γ , δ relate to the potential of each oxide to remove CO₂ from the atmosphere. At mildly acidic and circumneutral pH - $\alpha = 1$, $\beta = 1$, $\varepsilon = 1$, $\theta = 1$, $\gamma = -1$, $\delta = -1.5$ (Renforth, 2019). ω accounts for the outgassing of CO₂ via carbonate buffering in the ocean, based on the charge of the ion, as described in Renforth and Henderson (2017). For the purposes of this study, no outgassing is assumed throughout the document until it is discussed in Section 5.1.2. Therefore, for the purposes of the initial results provided, $\omega = 2$ to account for the two bicarbonates which are balanced by either a divalent cation or two monovalent cations. AppD

refers to the application rate of rock per unit area, which in this case, tons rock per ha. The resulting value, E_{pot} , in this instance is provided as tons of maximum CDR ha^{-1} .

2.6.2. Potential CDR from exchangeable cations

Cations adsorbed to soil exchange sites were used to calculate inferred pCDR (referred to as ExPot) using the following Equation 2:

$$ExPot = \left(\frac{((2 * (Mg^{2+} + Ca^{2+})) + Na^{+} + K^{+}) \cdot 44.01}{1,000,000} \right) \cdot (BD \cdot D \cdot 10,000) \quad (2)$$

Where Mg^{2+} , Ca^{2+} , Na^{+} and K^{+} relate to the respective exchangeable moles (in $mol\ kg^{-1}$) soil, BD is the bulk density (in $kg\ m^{-3}$), D equals the depth (in m). For this study, an average BD of $1,380\ kg\ m^{-3}$ across the 30 cm depth is assumed, based on bulk density measurements. The 1,000,000 converts grams to tons, and the 10,000 converts from m^2 to ha.

Inferred pCDR by was calculated by subtracting the control values (natural weathering) from the basalt amended values. This represents the ExPot values at a given time point, which may change seasonally (Dietzen and Rosing, 2023).

2.6.3. Potential CDR via pore water flux

The direct pCDR flux was calculated from porewater chemistry (as described in Section 2.1) and precipitation and evapotranspiration data. Evapotranspiration data (ET) was subtracted from the precipitation data (P) to calculate an assumed water flux being transported through the soil column (P-ET). For this calculation, the daily precipitation and reference evapotranspiration data at a resolution of 25 km was obtained from OpenMeteo, an open-source historical weather dataset which uses interpolation of neighboring weather stations to estimate weather conditions at any point on earth (Open-Meteo, 2025). Between any two porewater sampling time points, daily P-ET (in mm) was summed and converted to $L\ ha^{-1}$. During dry periods where ET exceeded P (i.e. $P-ET = 0$), it is assumed that there was no movement of fluid through the column, and therefore, no direct pCDR.

The concentration of bicarbonate at each sampling event was estimated by balancing the equivalents of Ca, Mg, Na and K with bicarbonate according to Equation 3 (McDermott et al., 2024):

$$[HCO_3^-] = ([Mg] + [Ca]) \cdot 2 + [K] + [Na] + ([Fe] + [Ba] + [Sr]) \cdot 2 - ([F] + [Cl] + [Br] + [NO_3] + ([SO_4] \cdot 2) + ([PO_4] \cdot 3)) \quad (3)$$

Where the elements in the equation are expressed in mol L⁻¹. During the study period, no PO₄ was detected, and Br was not measured - so both were omitted from the equation.

To obtain the flux of bicarbonate, the estimated bicarbonate concentration (mol HCO₃⁻ L⁻¹) was multiplied by the accumulated P-ET in the interim period between sampling events over one ha (L ha⁻¹) to obtain an area-normalized concentration of bicarbonate (mol HCO₃⁻ ha⁻¹) at a given measurement point. It is assumed that the bicarbonate calculated from one measurement point to the next has been transported beyond the measurement point (e.g. 5 or 10 cm depth). The results were then cumulated, to obtain a cumulative flux after a given number of weathering days. The cumulative flux was then converted to tons CO₂ ha⁻¹ by multiplying the results by 4.401_{x10}⁻⁵ mol ton⁻¹, thus accounting for the molecular mass of CO₂ (44.01 g mol⁻¹) and conversion between grams and tons.

The cumulative bicarbonate flux from the control results (representing natural carbon removal via weathering, not additional carbon removal) was subtracted from the bicarbonate fluxes of each basalt amended treatment to obtain a time-integrated direct pCDR estimate for the project period. For statistical analysis, the cumulated direct pCDR value after 576 days (18th April 2024) was used.

2.7 Statistical analysis

The cumulated bicarbonate flux between treatment plots relative to the control in both depths (5 and 10 cm) was evaluated statistically at the end of the porewater timeseries, after 576 days (*c.* 1.5 years). The overall effect of basalt amendment on the cumulated bicarbonate flux, estimated from porewater samples, was evaluated using a Generalized Linear Model (GLM) with a gaussian distribution family and treatment as a continuous explanatory variable. The estimated inferred pCDR from exchangeable cations, ExPot, was also evaluated using a GLM with a gaussian distribution family, but with treatment as a categorical and sampling date as a continuous explanatory variable. To account for inter-plot variability the mean ExPot in the baseline samples from each plot were subtracted from the ExPot at each monitoring sampling event. The model assumptions were evaluated using Shapiro-Wilk (for normality) and White's Lagrange multiplier test (for homoscedasticity). For the porewater

bicarbonate flux, soil sample ExPot and soil pH the difference between the control plot and the treated plots were evaluated using a Tukey's HSD post hoc test. Statistical analyses were carried out using Python (version 3.9) and the package Statsmodels (version 0.14.4, (Seabold and Perktold, 2010)).

3. Results

3.1. Porewater chemistry and flux data

The raw porewater concentration data for calcium, magnesium, sodium and potassium, as well as pH and electrical conductivity (EC) from both extraction depths are shown in Figure 3. Data for iron, barium, strontium, chloride, nitrate, sulphate and fluoride are plotted in Figure S2. Porewater pH varies between 3.6 and 7.6 (Figure 3a and g), and EC between 2.3 to 304.9 $\mu\text{S m}^{-1}$ (Figure 3b and h), respectively. The cation concentrations were ranked in descending order according to their magnitude as follows: calcium > sodium > magnesium > potassium.

Largely, higher calcium, magnesium and sodium concentrations were identified in basalt amended treatments (e.g. 126 > 78 > 23 > 0 t ha⁻¹). This trend is also evident in the magnesium and sodium time series, relative to calcium (Figure 3c, d, e, i, j and k), indicating weathering. Calcium concentration is often more variable in soils (Dietzen and Rosing, 2023), which could explain the greater variance in the measured calcium concentrations in the pore water. EC data also broadly follows the same trend of values in the plots that received basalt amendment (Figure 3b and h), indicating a measurable contribution of ions introduced by basalt weathering to the ionic strength of pore water solutions. Potassium concentrations are consistently higher and more variable at any given time point in the 78 t ha⁻¹ treatment relative to all the other treatments (Figure 3f and l).

The pH data are highly variable, with no discernible trends, suggesting the involvement of some kind of pH buffering reactions, involving organic carbon, for instance (Figure 3a and g).

The results of porewater concentration data converted into bicarbonate flux are presented in Figure 4. Data from the control plot indicate that natural bicarbonate fluxes vary between 0.438±0.09 and 0.656±0.321 tCO₂ ha⁻¹ in the 5 and 10 cm samples over the duration of the porewater time-series.

After 576 days of rock weathering, a strong overall dependency of basalt amendment on the cumulated bicarbonate flux was found at both 5 and 10 cm depth ($p < 0.001$ in the GLMs). The two models showed that the treatment accounted for a very large part of the variability in the cumulated bicarbonate flux, with pseudo R-square values of 0.99 and 0.65, for the 5 and 10 cm depth, respectively. The models met model assumptions.

Statistically significant increases in cumulative bicarbonate were observed between the control and the two high applications (78 and 126 t ha⁻¹, $p = 0.0037$ and $p = 0.0001$, respectively) in the porewater time series from 5 cm depth (Table 3). Despite the significant overall effect of basalt treatment on the cumulated bicarbonate flux in 10 cm, no individual pairwise comparison between the control and treated plots did not yield any significant results (Table 3). When comparing the control to the basalt amended treatments in treatments where significant differences were observed, the mean difference \pm std varied between 0.33 ± 0.11 and 0.53 ± 0.13 tCO₂ ha⁻¹ (Table 3) as direct pCDR.

3.2. Soil exchangeable cations (ExPot)

Major exchangeable cations (calcium, magnesium, sodium and potassium) and soil pH were determined on soil samples taken to a depth of 30 cm across the four plots (Figure 1) at five time points during this experiment. The sum of the major exchangeable cations is shown in Figure 5. The results indicate that there is high variability both within and between the plots. The variability appears to be the greatest in the spring and summer samples from 2023. Both the baseline and the samples from January 2025 were also analyzed for soil inorganic carbon, to track the precipitation of carbonates, but all results were below the detection limit.

Contrary to Figure 5, data from the single time point (July 2023) between control and 126 t ha⁻¹ when ExPot was calculated on composite samples from a 0-10 cm depth identified statistically significant increases in ExPot in the 126 t ha⁻¹ treatment relative to the control. Significantly higher concentrations of calcium and sodium in the high application plot ($p < 0.05$, ANOVA) and marginally higher magnesium, as well as marginally lower potassium (Supplementary Material Figure S3). Overall, this led to a statistically significant inferred pCDR of 1.909 tCO₂ ha⁻¹ (Supplementary Material Figure S3).

While the pH was significantly higher than the control in the two high application plots (78 and 126 t ha⁻¹) on the 23rd January 2023 (after *c.* 4 months) and 14th January 2025 (after *c.* 28 months), as well as for 126 t ha⁻¹ on the 18th April 2023 (after *c.* 7 months)

(Supplementary Material Table S2), no significantly higher ExPot is observed in any of the time points measured in this study between the control and any treatment (Supplementary Material Table S3). This suggests that the exchange pool represents a large pool of retained metal ions, by comparison with the metal concentrations in porewaters. In this scenario large relative changes in porewater concentrations would be accompanied by small relative changes in exchanger loadings.

3.3. Comparison between CDR methods

Even though no significant differences are observed in the ExPot, there was no inferred pCDR based on the 30 cm soil time series. The values for ExPot, which could be considered ‘natural’ pCDR if at some point they were removed from the exchangers and charge balanced bicarbonate, were *c.* 1 order of magnitude higher than direct pCDR measured from porewater at both 5 and 10 cm depths (Figure 6).

ExPot is also *c.* 1 order of magnitude lower than the theoretical maximum CDR values (Figure 6). The ExPot estimated for the 23 t ha⁻¹ treatment is close to E_{pot} value at the sampling event in July 2023, however ExPot data is very variable (Figure 6) and is likely an artifact of soil heterogeneity.

4. Discussion

4.1. Overall Experimental Drawbacks

A key limitation to the experimental design in this study is the absence of plot replication; there was only one plot per treatment. A range of experimental designs for EW studies have been published previously, including paired catchments (control and amended; e.g. Larkin et al., 2022; Taylor et al., 2021), strip designs (e.g. Holden et al., 2024), split field designs (e.g. McDermott et al., 2024) and randomized block designs (e.g. Deng et al., 2024; Stubbs et al., 2025). These experimental designs are typically more statistically robust than the experimental design used to generate data in this study.

The experimental design presented in this study was initially designed to investigate whether pH and EC sensors could be used to fill the temporal gaps between porewater sampling events. Hence, the rhizon samplers were installed in soil pits in close proximity with the soil sensors with the aim of identifying empirical relationships between soil sensor data and porewater sample results. A key advantage of sensor-based measurements is that

they would generate continuous data, rather than at discrete time intervals, which could be used to extrapolate direct pCDR using precipitation surplus (P-ET) data, as presented here. This is discussed in detail in Section 4.2. Due to the cost of sensor installation and the requirement for a central data logger for each 10 sensor pairs of pH and EC sensors, it was not financially feasible to install sensors across replicated plots. Unfortunately, the acquisition of soil sensor data was terminated due to vandalism at the experimental site.

Suitable porewater baseline samples would require multi-year sampling to account for both seasonal and inter-year variability. However, obtaining initial porewater samples before the rock was applied would have been useful for ensuring the soil had re-equilibrated following rhizon installation and for confirming whether, for a short period before the experiment took place, that the plots were statistically similar to each other. There were significant differences in the baseline soil samples for exchangeable calcium and magnesium as these were the only two variables which were significantly different in the baseline samples. However, the mean \pm std for exchangeable calcium and magnesium varied by only 7 and 10% between the baseline samples.

4.2. Porewater data

Direct pCDR from cumulative porewater was significantly explained by the application of basalt in both 5 and 10 cm depth (GLM, $p < 0.001$), at the end of the 1.5 year long porewater time series. Where treatments were statistically different from the control in the 5 cm sampling depth (78 and 126 t ha⁻¹), linearity is observed between the tons of rock applied and percentages of CDR (Table 3) with mass-normalized-pCDR of 0.0042 tCO₂ ha⁻¹ tRock⁻¹. The GLM calculated pseudo r^2 values of 0.999 between the three basalt amended treatments, however, caution should be taken when assessing linearity using only two statistically significant data points.

The results also indicate that direct pCDR observed in the porewater accounts for only a small amount of the maximum theoretical CDR calculated through the E_{pot} equation - between 1.1% and 1.72%. These low percentages may indicate low weathering rates. In this experiment, the feedstock was not amended into the soil profile, but was surface-applied on the grassland and therefore was not exposed to the higher $p\text{CO}_2$ observed in soil profiles (e.g. Nan et al., 2016). Moreover, the feedstock applied in this study was coarse grained with a D_{50} of 1,006 μm (e.g. Figure S1). Additionally, this could be because the theoretical maximum CDR does not take rock dissolution kinetics into account. Rock dissolution rates are

influenced by the amendment's SSA (which in turn is influenced by particle size and mineralogy; Lewis et al., 2021) and mineralogy (e.g. structural location of the base cations), while E_{pot} values only use whole rock chemistry. These results confirm that it is not appropriate to use E_{pot} values to predict CDR in agricultural EW studies over annual timescales. It is not possible to test at what time scale an E_{pot} value is appropriate for, however, the value could be useful for comparing feedstock to select appropriate rock sources (Clarkson et al., 2024).

There are some limitations to using a porewater time series alone for direct pCDR estimations, and the results presented in this paper most likely represent the minimum direct pCDR over the measurement period. While the determination of the soil porewater concentration of bicarbonate at a particular point in time is the most direct measure of the instantaneous pCDR reservoir in the topsoil (Clarkson et al., 2024), using these measurements for temporal extrapolation have limitations including: (1) seasonal variability, (2) limited sampling duration and frequency and (3) practical limitations. Seasonal variability in both the water flux through the soil (i.e. the transport of CDR products to the groundwater, Figure 2) and porewater concentrations (Figure 3) were observed in this study, with Δ bicarbonate varying by *c.* 2 orders of magnitude between time points over the year (Figure 4). This implies that the timing of porewater sampling in relation to rain events is pivotal to avoid missing a signal. Time series analysis has shown strong correlation ($r^2 = 0.57$, $p = 0.0014$) between rainfall averaged over a 10-day period prior to sampling and porewater cation concentrations (Betz et al., 2025). As the porewater sampling takes place over *c.* 24 to 48 hours approximately every two weeks (in periods of sufficient soil moisture to extract porewater), the sampling period represents <14% of the total time integrated.

Additionally, the first porewater samples were taken 25 days after the rock application, due to insufficient soil moisture for porewater collection. Between the time of rock application and the first measurement, the fields were subjected to a total water flux (P-ET) of 106 mm. An initial weathering signal resulting from the dissolution of finer particles and high SSA asperities may have been missed (Power et al., 2025) and therefore direct pCDR may have been underestimated.

Even if the sampling timing is based on analysis of the relationship between rain events and porewater concentration (Betz et al., 2025), the logistical challenge in collecting soil porewater is primarily governed by the availability of sufficient water yield. A potential

solution for the latter utilizes centrifugation of soil samples (e.g. (Jones et al., 2025)). Integrating different instrumentation, such as passive wick drainage flux meters (as implemented in Holden et al., 2024) or hydrologically isolated plots which both collect water continuously may avoid these issues. Soil porewater extraction is notoriously known to be labor-intensive with no guarantee of porewater yield, as samplers may lose vacuum or be ineffective at low moisture levels, leading to insufficient volumes of sample obtained for chemical analysis. The macro rhizons used in this study to collect porewater are also considered consumable, with an expected lifespan from the manufacturers stated as six months. Dry summers and cold winters affected the longevity of the rhizons in this study, but replacement is carried out with minimal disturbance.

Despite these drawbacks in the experimental data, the method to calculate flux based on daily, rather than monthly or annual, precipitation surplus data (P-ET), is likely to provide a more accurate indication of direct pCDR due to seasonality (e.g. Figure 2). Furthermore, as stated above, correlation data between rainfall averaged over 10-day periods also suggests that monthly P-ET values may not be sufficient when integrating precipitation surplus and concentration data to obtain direct pCDR estimates. This method could be improved in future iterations by incorporating soil hydrology into flux calculations.

4.3. Soil Data

Overall, no statistically significant changes were observed in the ExPot, which is likely a result of the experimental set-up and sampling design. The concentration of exchangeable cations in the soil samples taken in the treated plots was not significantly higher than in the control in any of the monitoring sample events (Figure 5 and 6, and Supplementary Material Table S3). This is despite soil pH readings appearing different for the highest application rate on several occasions (Figure 5), no statistically significant results confirmed this trend (Supplementary Material Table S2). Several potential reasons for the lack of differences in the inferred pCDR stored on the soil exchangers have been identified, including: (1) inherent soil variability, (2) spreading heterogeneity, (3) basalt application strategy and (4) sampling frequency. The variability in exchangeable cations observed in this study suggests that compositing of multiple samples into one may be useful in decreasing within treatment sample variability. The soil samples were taken within the greater plot boundaries where basalt was applied using a commercial lime spreader. Due to the inherent variability in spreading rate when using commercial equipment, it is likely that differences between the

plots may have been discernible had the sampling density been higher. Additionally, the accumulation and flushing of inferred pCDR on exchangeable cations is likely to be time sensitive (Dietzen and Rosing, 2023), so infrequent sampling may have missed the accumulation peak before flushing.

The basalt was surface-applied during this study, i.e. not incorporated into the soil, so there is a high risk that any topsoil differences will not be detectable due to dilution with the deeper soil. This is evidenced from the singular time point tested in July 2023, where five composite samples each comprising 20 subsamples were taken to a depth of 10 cm from the control and 126 t ha⁻¹ plots, respectively. These values identified an ExPot inferred pCDR of 1.909 tCO₂ ha⁻¹ (Supplementary Material Figure S3), without accounting for the deduction factors which are briefly discussed in Section 4.4.

4.4. CDR Deductions

The direct pCDR values presented so far assume that all the pCDR calculated in the porewater will remain in solution. However, outgassing from riverine (i.e. equilibration of soil water into riverine water (Zhang et al., 2022, 2025; Harrington et al., 2023) and oceanic outgassing (due to carbonate buffering, (Renforth and Henderson, 2017) can reduce CDR efficacy by 22% (Table 4). Riverine losses and ocean losses are likely to be highly dependent on catchment/environmental conditions (Zhang et al., 2022; Harrington et al., 2023), however, a factor of 5% is applied in this study based on results from Zhang et al. (2025). Oceanic carbonate buffering will reduce the CDR efficacy by 13-17% (Renforth and Henderson, 2017), depending on ocean temperature, salinity and atmospheric CO₂ concentrations.

Strong acid weathering is already excluded when calculating alkalinity by charge balance via Equation 3, but to calculate the net CDR from porewater data, additional deductions need to be taken for plant uptake. Plant uptake could have occurred in this trial because grass species typically root down to 10 cm depth (Schenk and Jackson, 2002), and therefore the cations measured during this study (particularly K), could be taken up by plants. However, the site was intermittently grazed and no grass cuttings were taken during the duration of the trial to confirm this. Moreover, grazing did not occur directly above the porewater rhizon samplers, as the central parts of the plots were fenced off. Hence any uptake of cations in the grass would be returned to the soil at senescence and therefore grass yields and chemistry were not determined. In addition to appropriate deductions for losses and leakages, a full life cycle

analysis of all emissions associated with activities during the project lifetime would also have to be conducted to calculate net CDR (e.g. Puro, 2022; Sutherland et al., 2024).

4.5. CDR comparisons with other field studies

The estimated direct pCDR, based on porewater data in this study (0.257 - 0.413 tCO₂ ha⁻¹, Table 4), sits within the range of published data (0.025 - 0.55 tCO₂ ha⁻¹, Table 5) from previous EW studies presenting aqueous sampling to deduce CDR (Kukla et al., 2024). However, there are challenges when comparing different EW studies due to the variety of climatic, soil and rock conditions used in field trials data. Given that a linear relationship between application rate and direct pCDR was observed in this study, inter-study CDR comparisons are discussed after being normalized per ton of rock applied and per year (tCO₂ ha⁻¹ tRock⁻¹ yr⁻¹ - and referred to as mass-time-normalized). Caution should be taken when interpreting mass-time-normalized CDR (or pCDR) or extrapolating further than simple comparisons; linear relationships are not always observed in enhanced weathering studies (Rijnders et al., 2024) and only three data points are used to interpret this trend (two significant). Additionally, within the published studies cited in Table 5, several were subject to repeat basalt applications. Where measurements are taken at depths below 1 m depth (e.g. well below the NFZ), CDR is referred to as CDR while above 30 cm depth follows the same nomenclature as the results provided in this study and is referred to as direct pCDR.

Both McDermott et al. (2024) and Deng et al. (2024) use P-ET to calculate direct pCDR/CDR fluxes, while Holden et al. (2024) use passive wick drainage flux lysimeters. High mass-time-normalized direct pCDR (up to 0.088 tCO₂ ha⁻¹ tRock⁻¹ yr⁻¹) of *c.* 1-4 orders of magnitude higher than other studies listed in Table 5 were observed in McDermott et al (2024). The fast dissolution kinetics of calcite, *c.* five orders of magnitude faster than labradorite which comprise 43.8 wt.% of the basalt used in this study, likely explains why the mass-time-normalized direct pCDR was higher. Deng et al., (2024) observed a similar amount of mass-time-normalized CDR (0.0023 tCO₂ ha⁻¹ tRock⁻¹ yr⁻¹) to the direct pCDR study (0.0021 tCO₂ ha⁻¹ tRock⁻¹ yr⁻¹). There are similarities in the soil used in this study compared with Deng et al (2024) (pH = 6.6; soil texture = silty loam/silty clay loam) and rock amendment used (basalt, with a *p*80 of 1050 μm). However, leachate samples were collected from 1 m depth - up to 20 times deeper than the porewater extraction depth presented in this study. In Holden et al (2024), non-carbonic acid weathering was reported to

drive over 98% of weathering and therefore, coupled with deep flux meter installation, low and statistically insignificant ($p = 0.082$) bicarbonate fluxes were observed.

Both Taylor et al (2022) and Larkin et al (2021) utilized river discharge to determine CDR. Firstly, three years of annual applications of 50 t ha^{-1} of basaltic andesite, CDR determined from alkalinity in river discharge was unresolvable in two out of three paired catchments when comparing control to amended paired catchments (Larkin et al., 2022). However, the paired catchment which showed $c.1 \text{ tCO}_2 \text{ ha}^{-1}$, converts to mass-time-normalized CDR of $0.022 \text{ tCO}_2 \text{ ha}^{-1} \text{ tRock}^{-1} \text{ yr}^{-1}$ which is of a similar order of magnitude as observed in Deng et al (2024). After applying a lower rate application (3.44 t ha^{-1}) of wollastonite amendment to a catchment which was monitored for 15 years, modest mass-time-normalized CDR of between $0.0005\text{-}0.0025 \text{ tCO}_2 \text{ ha}^{-1} \text{ tRock}^{-1} \text{ yr}^{-1}$ was observed.

River transport is quicker than groundwater transport (Dingman, 2002) so once the charge-balanced bicarbonate is transported into rivers, and after the initial outgassing and assuming that no more outgassing will occur along a river course, it could reach the ocean quickly. However, it can take time for weathering products to be transported to rivers, and weathering products may remain in groundwater for millennia. Many of the CDR/pCDR data used in this study are taken at depths greater than 1 m which is considerably larger than the near field zone as defined in methodologies (e.g. Sutherland, 2024; Puro, 2024; Mills et al., 2024). At deeper depths, outgassing, and the potential for plant uptake may not be such an issue. Even so, more research is needed to identify the time point under different hydrological conditions where dissolved and charge balanced bicarbonate is at low risk of outgassing, or outgassing during throughflow until the water table is constrained.

Aqueous phase measurements from studies compared in this section are typically one order of magnitude lower than ‘natural’ pCDR measurements derived from soil- and mass-balance-based approaches. Mass-time-normalized soil-based calculations report values of inferred pCDR of $0.013 \text{ tCO}_2 \text{ ha}^{-1} \text{ tRock}^{-1} \text{ yr}^{-1}$ when four annual applications of 50 t ha^{-1} basalt (e.g. 200 t ha^{-1} at the time of measurement) were applied to maize-soy rotations in the Midwest USA (Beerling et al., 2024). Tropical ERW measurements reported by InPlanet during their carbon credit verification by Isometric obtained mass-time-normalized inferred pCDR values of $0.018 \text{ tCO}_2 \text{ ha}^{-1} \text{ tRock}^{-1} \text{ yr}^{-1}$ when applying 10 t ha^{-1} of basalt and measuring after one year (Isometric HQ Ltd, 2025). While no statistically significant inferred pCDR via soil sample measurement was observed in this study, ‘natural’ pCDR were similarly one

order of magnitude higher than porewater flux-based direct pCDR, as observed in these two examples described above. One reason for the discrepancy between porewater and mass-balance approaches could be that a time lag between weathering and the observation of increased cations in the leachate following the adsorption of cations onto soil exchange sites (e.g. Kanzaki et al., 2024). However, the isometric methodology aims to account for these differences through the measurement of different cation sinks in the agricultural system (Sutherland et al., 2024).

The time-mass-normalized direct pCDR reported in this study ($0.0021 \text{ tCO}_2 \text{ ha}^{-1} \text{ tRock}^{-1} \text{ yr}^{-1}$) is within the midrange of time-mass-normalized results reported in Table 5 ($0.001 - 0.088 \text{ tCO}_2 \text{ ha}^{-1} \text{ tRock}^{-1} \text{ yr}^{-1}$). The study did take place in temperate climates, using relatively slow weathering feedstocks (e.g. basalt). Other feedstocks, such as wollastonite, and regions with warm, wet summers, would likely lead to faster weathering rates, as per common consensus on dissolution kinetic laws (e.g. Palandri and Kharaka, 2004). However, slower weathering feedstocks could be significant over decadal (e.g. 20-year) timescales and this study suggests that detecting signals in slow weathering materials can be challenging, particularly at lower application densities, but aided by high-frequency and/or time integrated measurements.

5. Conclusions

Integrating daily P-ET fluxes with measured porewater concentrations at 5 and 10 cm depth over 1.5 years of weathering produced statistically significant direct pCDR. Significant direct pCDR of up to $0.53 \text{ tCO}_2 \text{ ha}^{-1}$ was observed when 126 t ha^{-1} basalt was applied to grassland soils. In general, during this field trial, direct pCDR increased linearly with application rate. This meant the equivalent of $42 \text{ kgCO}_2 \text{ tRock}^{-1} \text{ ha}^{-1}$ ($0.0042 \text{ tCO}_2 \text{ ha}^{-1} \text{ tRock}^{-1}$) were potentially removed following 1.5 years of weathering. These values are *c.* 2 orders of magnitude lower than the theoretical maximum CDR - confirming that maximum theoretical CDR is not a useful indicator of CDR over short timescales but can serve as a useful tool to compare the potential of different feedstocks. Although direct pCDR measured from porewater sampling is the most direct measure of CDR via EW, discontinuous sampling methods could underestimate pCDR. However, slower weathering feedstocks could be significant over decadal (e.g. 20-year) timescales and this study suggests that detecting signals in slow weathering materials can be challenging, particularly at lower application densities, but aided by high-frequency and/or time integrated measurements.

6. References

Amann, T., Hartmann, J., Hellmann, R., Pedrosa, E.T. and Malik, A. (2022). Enhanced weathering potentials—the role of in situ CO₂ and grain size distribution. *Frontiers in Climate*, 4. Available at:

<https://www.frontiersin.org/journals/climate/articles/10.3389/fclim.2022.929268>.

Amiotte Suchet, P., Probst, J.-L. and Ludwig, W. (2003) .Worldwide distribution of continental rock lithology: Implications for the atmospheric/soil CO₂ uptake by continental weathering and alkalinity river transport to the oceans. *Global Biogeochem Cycles*, 17. doi: <https://doi.org/10.1029/2002GB001891>.

Beck, H.E., Zimmermann, N.E., McVicar, T.R., Vergopolan, N., Berg, A. and Wood, E.F. (2018). Present and future Köppen-Geiger climate classification maps at 1-km resolution. *Sci Data*, 5, 180214. doi: 10.1038/sdata.2018.214.

Beerling, D.J., Leake, J.R., Long, S.P., Scholes, J.D., Ton, J., Nelson, P.N., et al. (2018). Farming with crops and rocks to address global climate, food and soil security. *Nat Plants*, 4, 138–147. doi: 10.1038/s41477-018-0108-y.

Beerling, D.J., Kantzas, E.P., Lomas, M.R., Wade, P., Eufrazio, R.M., Renforth, P., et al. (2020). Potential for large-scale CO₂ removal via enhanced rock weathering with croplands. *Nature*, 583, 242–248. doi: 10.1038/s41586-020-2448-9.

Beerling, D.J., Epihov, D.Z., Kantola, I.B., Masters, M.D., Reershemius, T., Planavsky, N.J., et al. (2024). Enhanced weathering in the US Corn Belt delivers carbon removal with agronomic benefits. *Proceedings of the National Academy of Sciences*, 121, e2319436121. doi: 10.1073/pnas.2319436121.

Berner, E.K. and Berner, R.A. (2012). *Global Environment*. Princeton University Press. doi: 10.1515/9781400842766.

Betz, J., Albahri, T., Cazzagon, G., Healey, M., Radkova, A., Solpuker, U., et al. (2025). Cation Release Dynamics in Basalt-Amended Soils: Implications for Enhanced Rock Weathering. doi: 10.22541/essoar.173939581.19736603/v1

Brunner, C., Hausfather, Z. and Knutti, R. (2024). Durability of carbon dioxide removal is critical for Paris climate goals. *Commun Earth Environ*, 5, 645. doi: 10.1038/s43247-024-01808-7.

Buss, W. and Hasemer, H. (2024). Measuring enhanced weathering: inorganic carbon-based approaches may be required to complement cation-based approaches. *Frontiers in Climate*, 6. Available at:

<https://www.frontiersin.org/journals/climate/articles/10.3389/fclim.2024.1352825>.

CDR.fyi. (2025). Carbon Removal Map. Available at: <https://www.cdr.fyi/carbon-removal-map>. [Accessed 4 April 2025]

Deng, F., James, R.H., Dunham, S., Hernandez, J., Herbin, C., Carter, J., et al. (2024). Quantifying carbon dioxide removal via enhanced rock weathering at an arable cropland field

trial in the UK. In: *2024 Goldschmidt Conference*, Goldschmidt. doi: <https://doi.org/10.46427/gold2024.22677>

Dietzen, C. and Rosing, M.T. (2023). Quantification of CO₂ uptake by enhanced weathering of silicate minerals applied to acidic soils. *International Journal of Greenhouse Gas Control*, 125, 103872. doi: <https://doi.org/10.1016/j.ijggc.2023.103872>.

Dingman, S. L. (2002). "Physical Hydrology," (Upper Saddle River, N.J. : Prentice Hall), 331.

Haque, F., Santos, R.M. and Chiang, Y.W. (2020). CO₂ sequestration by wollastonite-amended agricultural soils – An Ontario field study. *International Journal of Greenhouse Gas Control*, 97, 103017. doi: <https://doi.org/10.1016/j.ijggc.2020.103017>.

Harrington, K.J., Hilton, R.G. and Henderson, G.M. (2023). Implications of the Riverine Response to Enhanced Weathering for CO₂ removal in the UK. *Applied Geochemistry*, 152, 105643. doi: <https://doi.org/10.1016/j.apgeochem.2023.105643>.

Hartmann, J., West, A.J., Renforth, P., Köhler, P., De La Rocha, C.L., Wolf-Gladrow, D.A., et al. (2013). Enhanced chemical weathering as a geoengineering strategy to reduce atmospheric carbon dioxide, supply nutrients, and mitigate ocean acidification. *Reviews of Geophysics*, 51, 113–149. doi: <https://doi.org/10.1002/rog.20004>.

Heřmanská, M., Voigt, M.J., Marieni, C., Declercq, J. and Oelkers, E.H. (2022). A comprehensive and internally consistent mineral dissolution rate database: Part I: Primary silicate minerals and glasses. *Chem Geol*, 597, 120807. doi: <https://doi.org/10.1016/j.chemgeo.2022.120807>.

Holden, F.J., Davies, K., Bird, M.I., Hume, R., Green, H., Beerling, D.J., et al. (2024). In-field carbon dioxide removal via weathering of crushed basalt applied to acidic tropical agricultural soil. *Science of The Total Environment*, 955, 176568. doi: <https://doi.org/10.1016/j.scitotenv.2024.176568>.

Isometric HQ Ltd. (2025). 235.53 tCO₂e removal by InPlanet. Available at: https://registry.isometric.com/removal/rmv_1J854R4NN1S05AYQ?tab=calculation-view. [Accessed 4 April 2025]

Jones, G., Zhang, Z., Clayton, K., Lancaster, L., Paschalis, A., and Waring, B. G. (2025). Utilizing soil centrifugation for accurate estimates of carbon dioxide removal via enhanced rock weathering. doi: 10.21203/rs.3.rs-6271461/v1

Jorat, M.E., Kraavi, K.E. and Manning, D.A.C. (2022). Removal of atmospheric CO₂ by engineered soils in infrastructure projects. *J Environ Manage*, 314, 115016. doi: <https://doi.org/10.1016/j.jenvman.2022.115016>.

Kantola, I.B., Masters, M.D., Beerling, D.J., Long, S.P. and DeLucia, E.H. (2017). Potential of global croplands and bioenergy crops for climate change mitigation through deployment for enhanced weathering. *Biol Lett*, 13, 20160714. doi: 10.1098/rsbl.2016.0714.

Kantzas, E.P., Val Martin, M., Lomas, M.R., Eufrazio, R.M., Renforth, P., Lewis, A.L., et al. (2022). Substantial carbon drawdown potential from enhanced rock weathering in the United Kingdom. *Nat Geosci*, 15, 382–389. doi: 10.1038/s41561-022-00925-2.

Kanzaki, Y., Planavsky, N., Zhang, S., Jordan, J., Suhroff, T.J. and Reinhard, C.T. (2024). Soil cation storage as a key control on the timescales of carbon dioxide removal through enhanced weathering. *Earths Future*.

Kelland, M.E., Wade, P.W., Lewis, A.L., Taylor, L.L., Sarkar, B., Andrews, M.G., et al. (2020). Increased yield and CO₂ sequestration potential with the C₄ cereal *Sorghum bicolor* cultivated in basaltic rock dust-amended agricultural soil. *Glob Chang Biol*, 26, 3658–3676. doi: <https://doi.org/10.1111/gcb.15089>.

Kukla, T., Tuhrhoff, T.J., Loeffler, S., Martin, K. and Chay, F. (2024). Does enhanced weathering work? We're still learning. *CarbonPlan*. Available at: <https://carbonplan.org/research/enhanced-weathering-fluxes>. [Accessed 4 April 2025]

Larkin, C.S., Andrews, M.G., Pearce, C.R., Yeong, K.L., Beerling, D.J., Bellamy, J., et al. (2022). Quantification of CO₂ removal in a large-scale enhanced weathering field trial on an oil palm plantation in Sabah, Malaysia. *Frontiers in Climate*, 4. Available at: <https://www.frontiersin.org/journals/climate/articles/10.3389/fclim.2022.959229>.

Lewis, A.L., Sarkar, B., Wade, P., Kemp, S.J., Hodson, M.E., Taylor, L.L., et al. (2021). Effects of mineralogy, chemistry and physical properties of basalts on carbon capture potential and plant-nutrient element release via enhanced weathering. *Applied Geochemistry*, 132, 105023. doi: <https://doi.org/10.1016/j.apgeochem.2021.105023>.

McDermott, F., Bryson, M., Magee, R. and van Acken, D. (2024). Enhanced weathering for CO₂ removal using carbonate-rich crushed returned concrete; a pilot study from SE Ireland. *Applied Geochemistry*, 169, 106056. doi: <https://doi.org/10.1016/j.apgeochem.2024.106056>.

Mignone, B.K., Clarke, L., Edmonds, J.A., Gurgel, A., Herzog, H.J., Johnson, J.X., et al. (2024). Drivers and implications of alternative routes to fuels decarbonization in net-zero energy systems. *Nat Commun*, 15, 3938. doi: 10.1038/s41467-024-47059-0.

Mills, J.V., Sanchez, J., Olagaray, N.Y., Wang, H. and Tune, A.K. (2024). Foundations for Carbon Dioxide Removal Quantification in ERW Deployments. *Cascade Climate*. Available at: https://cascadecclimate.org/CC_Foundations%20for%20CDR%20Quantification%20in%20ERW%20Deployments.pdf [Accessed 4 April 2025].

Nan, W., Yue, S., Li, S., Huang, H. and Shen, Y. (2016). The factors related to carbon dioxide effluxes and production in the soil profiles of rain-fed maize fields. *Agric Ecosyst Environ*, 216, 177–187. doi: <https://doi.org/10.1016/j.agee.2015.09.032>.

Open-Meteo. (2025). Open-Meteo Features. Available at: <https://open-meteo.com/en/features>. [Accessed 4 April 2025]

- Palandri, J.L. and Kharaka, Y.K. (2004). A Compilation of Rate Parameters of Water-Mineral Interactions Kinetics for Application to Geochemical Modeling. Menlo Park, California, US.
- Power, I. M., Hatten, V. N. J., Guo, M., Schaffer, Z. R., Rausis, K., and Klyn-Hesselink, H. (2025). Are enhanced rock weathering rates overestimated? A few geochemical and mineralogical pitfalls. *Frontiers in Climate* Volume 6-2024. Available at: <https://www.frontiersin.org/journals/climate/articles/10.3389/fclim.2024.1510747>
- Puro. (2022). Enhanced Rock Weathering: Methodology for CO₂ Removal, Puro Standard, 2022 Edition v. 2. [online] Available at: https://7518557.fs1.hubspotusercontent-na1.net/hubfs/7518557/ERW%20Standards/Enhanced_Rock_Weathering_2022_2.pdf [Accessed 4 April 2025].
- Renforth, P., Washbourne, C.-L., Taylder, J. and Manning, D.A.C. (2011). Silicate Production and Availability for Mineral Carbonation. *Environ Sci Technol*, 45, 2035–2041. doi: 10.1021/es103241w.
- Renforth, P. (2012). The potential of enhanced weathering in the UK. *International Journal of Greenhouse Gas Control*, 10, 229–243. doi: <https://doi.org/10.1016/j.ijggc.2012.06.011>.
- Renforth, P. and Henderson, G. (2017). Assessing ocean alkalinity for carbon sequestration. *Reviews of Geophysics*, 55, 636–674. doi: <https://doi.org/10.1002/2016RG000533>.
- Renforth, P. (2019). The negative emission potential of alkaline materials. *Nat Commun*, 10, 1401. doi: 10.1038/s41467-019-09475-5.
- Rijnders, J., Vienne, A. and Vicca, S. (2024). Effects of basalt, concrete fines, and steel slag on maize growth and heavy metal accumulation in an enhanced weathering experiment. *EGU sphere*, 2024, 1–34. doi: 10.5194/egusphere-2024-3022.
- Schenk, H.J. and Jackson, R.B. (2002). Rooting depths, lateral root spreads and below-ground/above-ground allometries of plants in water-limited ecosystems. *Journal of Ecology*, 90, 480–494. doi: <https://doi.org/10.1046/j.1365-2745.2002.00682.x>.
- Schulte, I., Burke, J., Arcusa, S., Mercer, L. and Hondeborg, D. (2024). “Chapter 10: Monitoring, Reporting and Verification, The State of Carbon Dioxide Removal - 2nd Edition,” in *The State of Carbon Dioxide Removal - 2nd Edition*, eds. S.M. Smith et al. Available at: <https://osf.io/adhp2/>.
- Seabold, S. and Perktold, J. (2010). Statsmodels: Econometric and statistical modeling with python. In: *Proceedings of the 9th Python in Science Conference*, Austin, 10–25080. 10.25080/Majora-92bf1922-011
- Skov, K., Wardman, J., Healey, M., McBride, A., Bierowiec, T., Cooper, J., et al. (2024). Initial agronomic benefits of enhanced weathering using basalt: A study of spring oat in a temperate climate. *PLoS One*, 19, e0295031-. Available at: <https://doi.org/10.1371/journal.pone.0295031>.

Smith, S.M., Geden, O., Gidden, M.J., Lamb, W.F., Nemet, G.F., Minx, J.C., et al. (2024). *The State of Carbon Dioxide Removal - 2nd Edition*. The State of Carbon Dioxide Removal. Available at: <https://osf.io/f85qj/>.

Stubbs, A., Tostevin, R., Healey, M., Skov, K., Turner, W., Cazzagon, G., et al. (2025). Evaluating Total Cation Accounting (TCA) as an MRV Approach for Enhanced Rock Weathering - Insights from a trial in Ontario, Canada. *EGU General Assembly 2025*, Vienna, Austria, 27 Apr–2 May 2025, EGU25-18780. doi: 10.5194/egusphere-egu25-18780.

Sutherland, K., Holme, E., Savage, R., Gill, S., Matlin-Wainer, M., He, J., et al. (2024). Enhanced Weathering in Agriculture v1.0. Available at: <https://registry.isometric.com/protocol/enhanced-weathering-agriculture/1.0#alternative-methods-and-approaches-for-determination-1>.

Taylor, L.L., Driscoll, C.T., Groffman, P.M., Rau, G.H., Blum, J.D. and Beerling, D.J. (2021). Increased carbon capture by a silicate-treated forested watershed affected by acid deposition. *Biogeosciences*, 18, 169–188. doi: 10.5194/bg-18-169-2021.

Warken, S.F., Riechelmann, D.F.C., Fohlmeister, J., Schröder-Ritzrau, A., Frank, N., Scholz, D., et al. (2024). Dynamic processes determine precipitation variability in Eastern Central Europe since the Last Glacial Maximum. *Commun Earth Environ*, 5, 694. doi: 10.1038/s43247-024-01876-9.

Wolff-Boenisch, D., Gislason, S.R. and Oelkers, E.H. (2006). The effect of crystallinity on dissolution rates and CO₂ consumption capacity of silicates. *Geochim Cosmochim Acta*, 70, 858–870. doi: <https://doi.org/10.1016/j.gca.2005.10.016>.

Zhang, S., Planavsky, N.J., Katchinoff, J., Raymond, P.A., Kanzaki, Y., Reershemius, T., et al. (2022). River chemistry constraints on the carbon capture potential of surficial enhanced rock weathering. *Limnol Oceanogr*, 67, S148–S157. doi: <https://doi.org/10.1002/lno.12244>.

Zhang, S., Reinhard, C.T., Liu, S., Kanzaki, Y. and Planavsky, N.J. (2025). A framework for modeling carbon loss from rivers following terrestrial enhanced weathering. *Environmental Research Letters*, 20, 024014. doi: 10.1088/1748-9326/ada398.

Figures

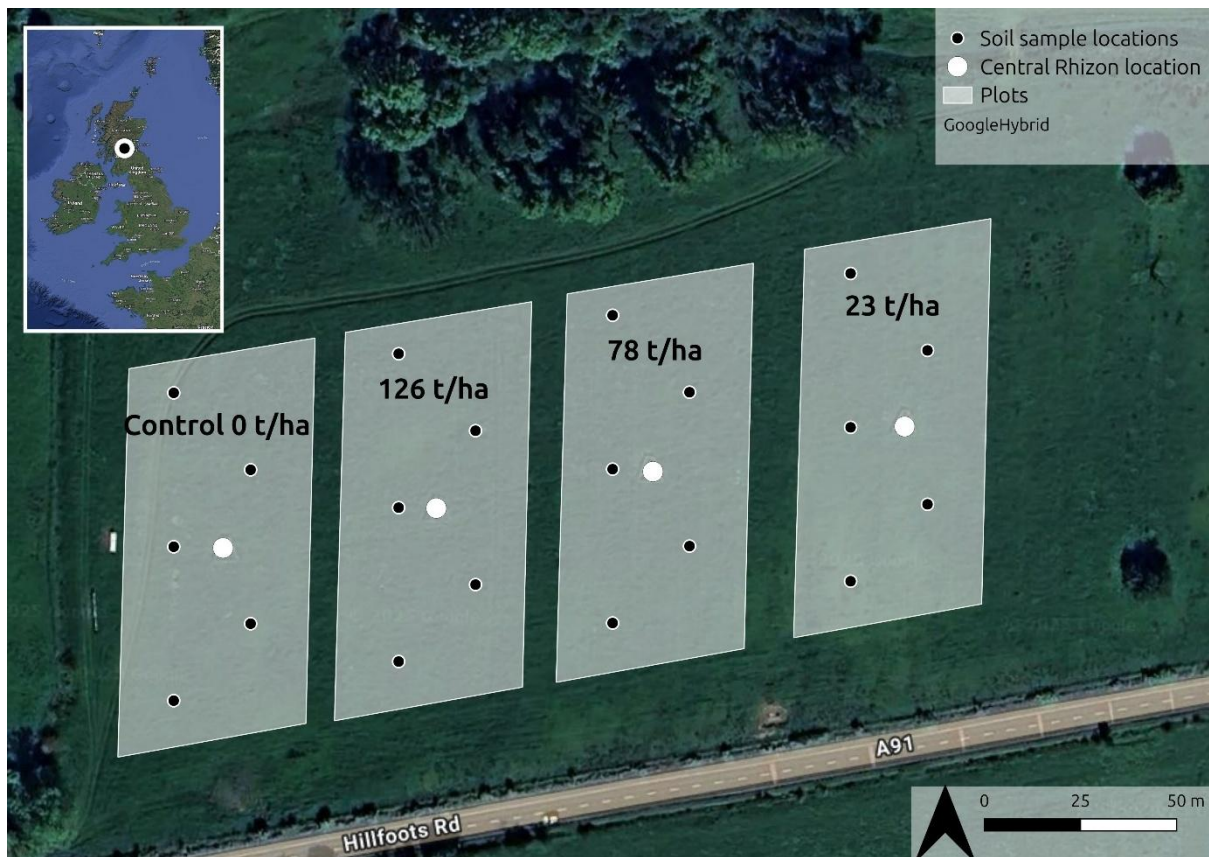


Figure 1. Overview of field trial layout with four *c.* half hectare plots. White circles indicate the location of the central soil pits in which rhizon samplers are installed in three separate pits. Black/white circles indicate the location of the soil samples. Background image and inset map image are GoogleHybrid with the WHS-84 coordinate reference system.

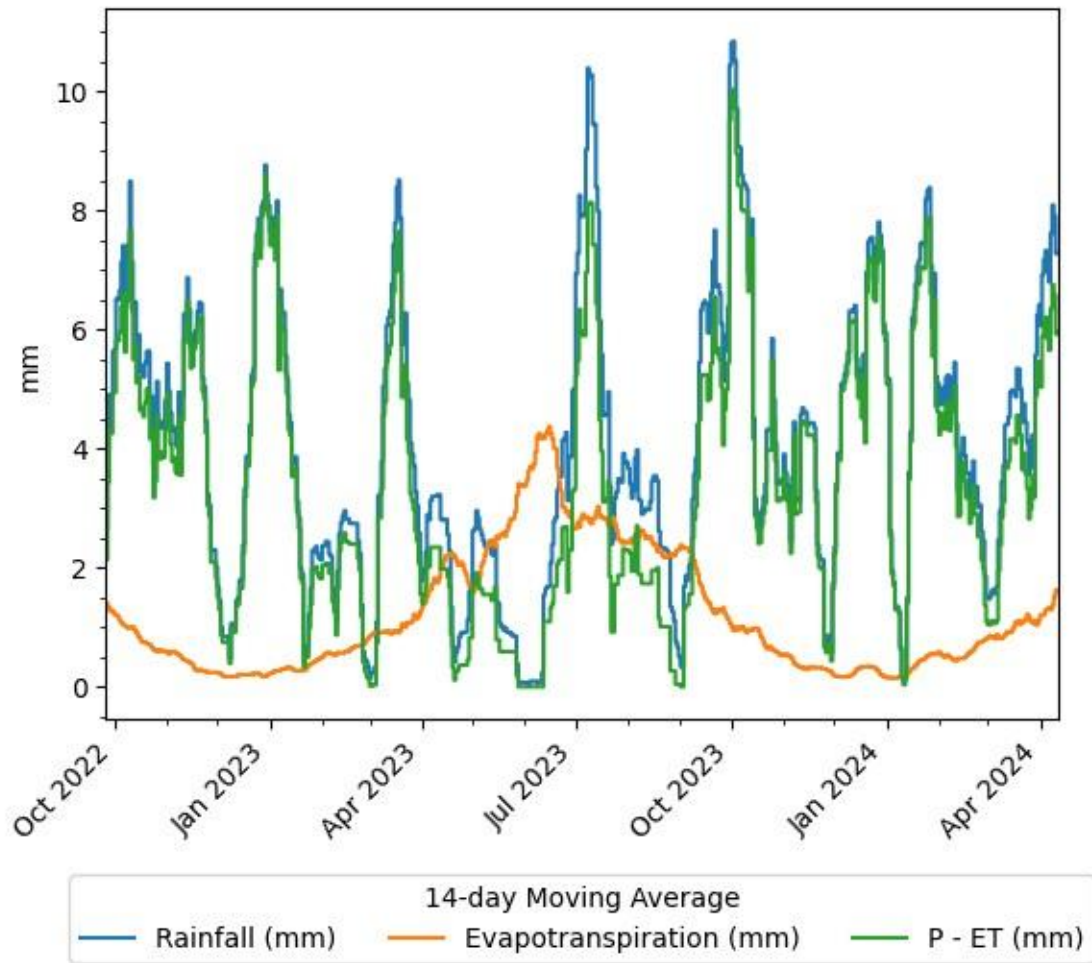


Figure 2. Precipitation and evapotranspiration data from Dumyat during the porewater data series (20th September 2022 – 18th April 2024), taken from Open-Meteo (Open-metro, 2025).

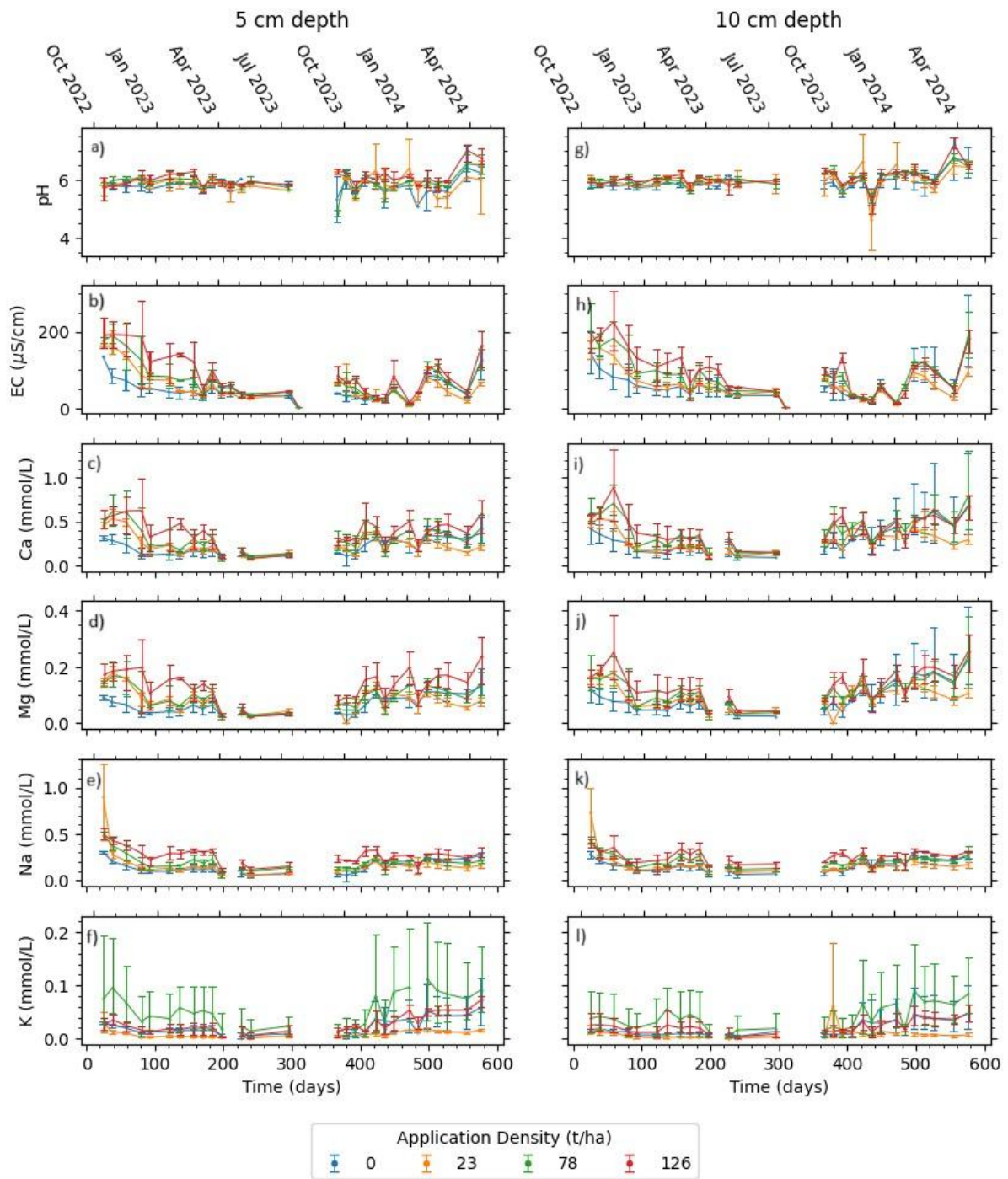


Figure 3. Porewater chemistry throughout the experimental duration at 5 cm depth (a-f) and 10 cm depth (g-l). Points represent mean values, and error bars represent minimum and maximum values ($n = 3$) for each sampling event.

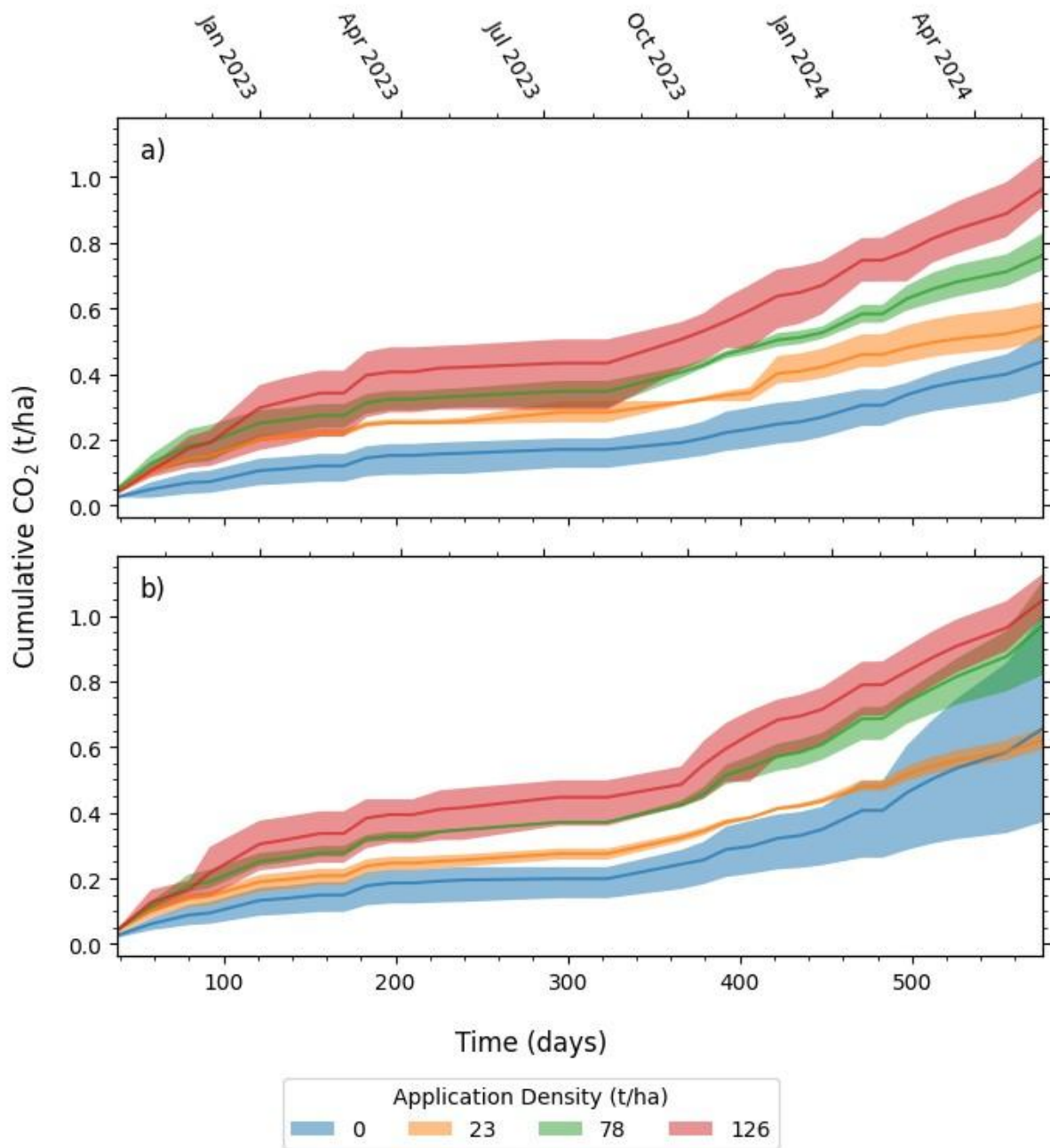


Figure 4. Cumulative direct potential CO₂ removal (direct pCDR), estimated using the charge balance equation described in Equation 3 from depths of 5 cm (a) and 10 cm (b). Data from 0 t ha⁻¹ represents non-additional CDR from background weathering.

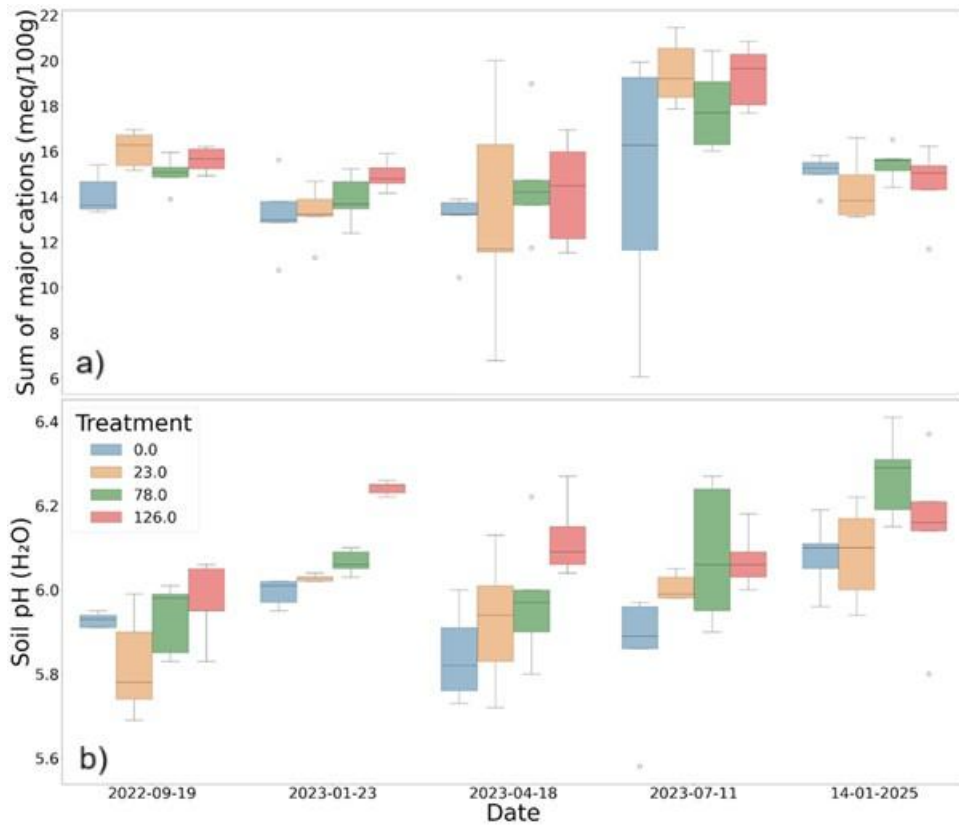


Figure 5. Sum of major cations (calcium, magnesium, potassium and sodium) in meq 100g⁻¹ in each plot and for each soil sampling event (a) pH (determined on a 1:2.5 ratio of soil to H₂O) (b).

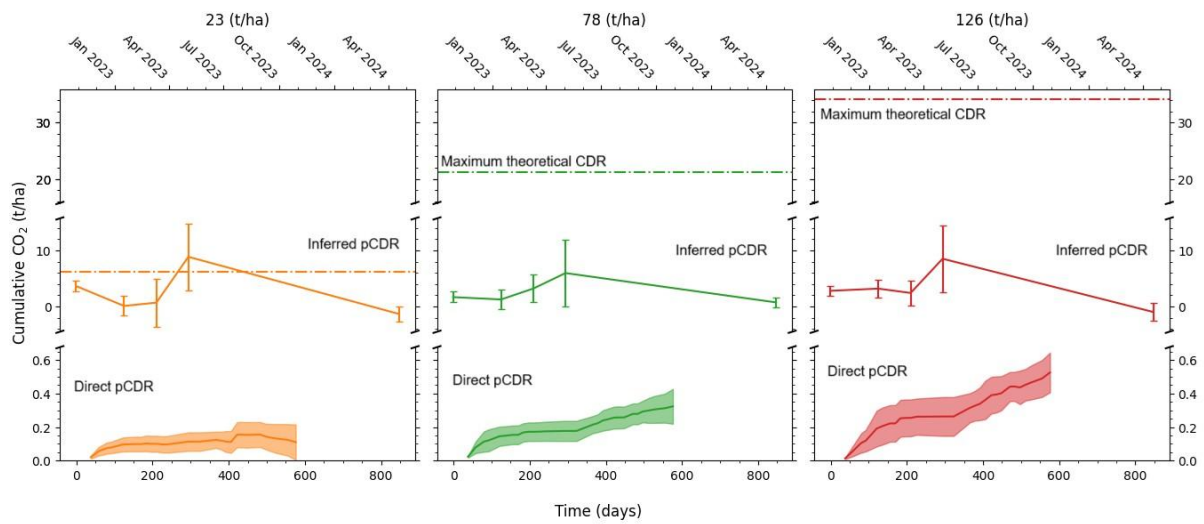


Figure 6. Comparison of potential CO₂ removal (pCDR) for the different basalt amended controls (23, 78 and 126 t ha⁻¹) with the control subtracted from the treatment, using three different methods (porewater flux (direct pCDR, cumulative curve with error envelope), exchangeable cations (inferred pCDR, point measurement with error bars) and maximum theoretical CDR (dashed line), to assess pCDR. Porewater was collected from 5 cm depth, while exchangeable cations came from soil data collected from the 0-30 cm depth.

1 **Tables**

2 **Table 1.** Mean and standard deviation of baseline soil sample results for soil texture (sand, silt, clay),
 3 soil organic carbon content (SOC), exchangeable calcium, magnesium, potassium and sodium, soil
 4 pH determined on a 1:2.5 ratio of soil and deionized water, bulk density (BD) in three different
 5 depths (5, 10 and 30 cm).

| Variable | Unit | Mean±Std |
|------------------------|------------------------|-------------|
| Sand | wt. % | 6.95±1.10 |
| Silt | wt. % | 57.90±0.72 |
| Clay | wt. % | 35.15±1.04 |
| SOC | wt. % | 3.55±0.37 |
| Exchangeable Calcium | meq 100g ⁻¹ | 12.22±0.86 |
| Exchangeable Magnesium | meq 100g ⁻¹ | 2.67±0.26 |
| Exchangeable Potassium | meq 100g ⁻¹ | 0.24±0.05 |
| Exchangeable Sodium | meq 100g ⁻¹ | 0.08±0.02 |
| pH [H ₂ O] | | 5.91±0.09 |
| BD [2.5 - 7.5 cm] | g cm ⁻³ | 1.089±0.066 |
| BD [7.5 - 12.5 cm] | g cm ⁻³ | 1.390±0.155 |
| BD [27.5 - 32.5 cm] | g cm ⁻³ | 1.665±0.076 |

6

7

8 **Table 2.** Measured rock mineralogy, accompanied by log-dissolution rate constants for the acidic
 9 (H⁺) and neutral (H₂O) dissolution rate mechanisms at 25°C. Rate constants are according to general
 10 dissolution rate equations set out in Palandri & Kharaka (2004) with dissolution rate constants also
 11 taken from Palandri & Kharaka (2004).

| Mineral | Formula | Wt. % | Rate Constant, A (H ⁺) | Rate Constant, A (H ₂ O) |
|-----------------------------------|---|-------|--|---|
| Fast weathering mineralogy | | | | |
| Labradorite | (Ca,Na)(Al,Si) ₄ O ₈ | 43.8 | -7.87 | -10.91 |
| Augite | (Ca,Na)(Mg,Fe,Al,Ti)(Si,Al) ₂ O ₆ | 18.7 | -6.82 | -11.97 |
| Ilmenite | FeTiO ₃ | 3.8 | -8.35 | -11.16 |
| Magnetite | Fe ₃ O ₄ | 3.6 | -8.59 | -10.78 |
| Slow weathering mineralogy | | | | |
| Chlorite | (Mg,Fe) ₅ Al(Si ₃ Al)O ₁₀ (OH) ₈ | 6.4 | -12.71 | -14.41 |
| Smectite | (Na,Ca) _{0.33} (Al,Mg) ₂ Si ₄ O ₁₀ (OH) ₂ ·nH ₂ O | 5.2 | -12.71 | -14.41 |
| Quartz | SiO ₂ | 7.5 | -13.99 | -16.29 |
| Unknown | | | | |
| Amorphous | Variable | 6.8 | - | - |
| Illite+Mica | K _{0.9} (Al,Fe,Mg) ₂ (Si ₄ O ₁₀)(OH) ₂ | 4.1 | - | - |

12

13

14

15 **Table 3.** Direct potential carbon dioxide removal (pCDR) from the 5 cm depth samples after 576
 16 days, as calculated by subtracting the control from basalt amended treatments. Mass-normalized
 17 direct pCDR is also calculated. Theoretical maximum CDR is calculated using the E_{pot} equation
 18 described in Equation 1. Statistically significant values ($p < 0.05$) are boldened.
 19

| Treatment, t ha ⁻¹ | Depth, cm | pCDR ¹ , tCO ₂ ha ⁻¹ (mean±std) | pCDR per tRock, tCO ₂ ha ⁻¹ tRock ⁻¹ | p-value | Theoretical maximum CDR per treatment (E_{pot} ·Treatment), tCO ₂ ha ⁻¹ | % Theoretical maximum reached |
|----------------------------------|-----------------|--|--|----------------|--|--|
| 23 | 5 | 0.11±0.11 | 0.0047 | 0.355 | 6.48 | 1.70% |
| | 10 ¹ | -0.035±0.32 | - ¹ | - ¹ | - ¹ | - ¹ |
| 78 | 5 | 0.33±0.11 | 0.0042 | 0.0037 | 21.96 | 1.50% |
| | 10 | 0.31±0.35 | 0.0039 | 0.222 | 21.96 | 1.41% |
| 126 | 5 | 0.53±0.13 | 0.0042 | 0.0001 | 34.48 | 1.54% |
| | 10 | 0.39±0.33 | 0.0030 | 0.1075 | 34.48 | 1.13% |

20 ¹Cumulative difference values are within standard deviation, so therefore no additional calculations
 21 were completed on this treatment.

22

23

24 **Table 4.** Direct potential carbon dioxide removal (pCDR) with a 22% deduction, as described in
 25 Section 4.4 applied. Statistically significant values ($p < 0.05$) are boldened. Note: CDR from 10 cm
 26 depth in the 23 t ha⁻¹ treatment are not included in this table as the CDR was within standard
 27 deviation limits of the natural CDR in the control.

| Application rate, t ha ⁻¹ | Depth, cm | pCDR (no correction factor), tCO ₂ ha ⁻¹ | pCDR with deductions, tCO ₂ ha ⁻¹ | Mass-Time-Normalized pCDR ¹ , tCO ₂ ha ⁻¹ tRock ⁻¹ yr ⁻¹ |
|---|--------------|---|--|--|
| 23 | 5 | 0.11 | 0.086 | 0.0024 |
| 78 | 5 | 0.33 | 0.257 | 0.0021 |
| 78 | 10 | 0.31 | 0.242 | 0.0020 |
| 126 | 10 | 0.53 | 0.413 | 0.0021 |
| 126 | 10 | 0.39 | 0.304 | 0.0015 |

28

29 **Table 5.** Comparison of different field studies quantifying carbon dioxide removal (CDR).

| Study | Rock amendment | Application density (t ha ⁻¹) | CDR (t CO ₂ ha ⁻¹) | CDR normalized (tCO ₂ ha ⁻¹ tRock ⁻¹ yr ⁻¹) | Measurement method/ depth | Experimental design |
|------------------------------------|---|--|--|---|--|--|
| McDermott et al (2024) | Crushed return concrete (construction by-product) | 7.5 | Up to 0.55 after 10 months | 0.088 | Suction cup lysimeters installed to 17.5 cm depth | Split field (n = 6 treatment, n = 2 control) |
| Deng et al., (2024) ¹ | Basalt (quarry by-product) | 40 annually for two years | 0.36±0.013 after 2 years of weathering | 0.00225 | Suction cup lysimeters installed to 100 cm depth | randomized block design (n = 3) |
| Larkin et al., (2022) | Basaltic andesite / andesite (quarry by-product) | 50 annually for three years | 1 in one paired catchment, no difference overall | 0.0022 in one paired catchment | Stream discharge | Paired hydrologically isolated catchments (n = 1, significant) |
| Taylor et al., (2021) | Crushed wollastonite | 3.44 | 0.025-1.3 after 15 years | 0.0005-0.0025 | Stream discharge | Paired hydrologically isolated catchments (n = 1) |
| Holden et al., (2024) ² | Basanite (quarry by-product) | 50 annually for 5 years | 0.026 tCO ₂ during 1 yr of measurement ³ | 0.0001 | Passive wick drainage flux meters installed at 125 cm depth | strip design (n=4) |
| Linke et al., (2024) ⁴ | Basaltic dust (natural) | 16,500 (c. 5 annually for 3,300 years) | 0.62±0.036 after 1 year | NA - uncertain contributions over 1 year | Suction cup lysimeters installed at 4 depths between 76 and 260 cm | singular site |

30 ¹from conference proceeding

31 ²not significant (p > 0.05)

32 ³HCO₃⁻ was only measured for one year, value used was therefore not divided by annual applications

33 ⁴natural analogue formed from volcanic eruptions

Supplementary Material

34 S1. Whole rock analysis (Taken from Skov et al. (2024))

35 Sample preparation

36 The samples used for Inductively Coupled Plasma- Atomic Emission Spectroscopy /- Mass
37 spectrometry (ICP-AES and ICP-MS) were prepared by ALS (Loughrea, Ireland). To create
38 representative samples, the sample was dried at 90°C and then crushed until greater than 70% of the
39 sample was less than 2 mm. A250 g rifle split of this dried and crushed material was then pulverized
40 using a LM2 pulverizing mill with B2000 steel bowls, and sieved until greater than 80% of the
41 material was less than 75 µm.

42 Determination of whole-rock mineralogy

43 A representative sample of Hillend basalt produced by ALS (dried at 70°C) was sent to X-ray
44 Mineral Services Laboratory (Colwyn Bay, UK) for X-ray diffraction (XRD) analysis, to determine
45 the whole rock mineralogy. The sample that was sent for analysis was then coned and quartered to
46 produce a representative sample with a weight of 20 g. This 20 g sample was disaggregated gently
47 using a pestle and mortar to homogenize the sample. The sample was then spiked with 10 g of <44
48 µm silicon powder at 99% purity (trace metals basis) (Sigma Aldrich, Germany) as an internal
49 standard to allow for the determination of the amorphous phase (interpreted in this case as basaltic
50 glass). Then, 2 g of the sample was micronized using a McCrone Micronizing Mill, using zirconium
51 elements to obtain a powder with individual particles between 5 and 10 µm in diameter. The resultant
52 slurry was dried overnight in an oven at 80°C, then re-crushed to a fine powder. The sample was
53 ‘backpacked’ into an aluminum cavity mount to produce a randomly oriented sample for whole rock
54 analysis. The XRD powder analysis was conducted with a Malvern Panalytical X’Pert3
55 diffractometer from 4.5 to 75°2θ using a CuKα radiation at 40 kV and 40 mA. The samples were
56 analyzed for 20 min with a step size of 0.013°. Rietveld analysis was then used to quantify the
57 mineralogy using the AUTOQUAN software, with crystallographic information files taken from the
58 ICDD PDF-4+ database. The mineralogy of the basalt determined using powder X-ray diffraction is
59 given in Table 1.

60 Determination of whole rock chemistry

61 The major oxide composition of the basalt was measured using X-Ray fluorescence (XRF) at ALS. A
62 0.66 g sample was prepared into a fused disk. The samples were then run using an XRF. Loss on
63 ignition (LOI) was also determined by ALS by heating the sample to 1000°C in a furnace. The XRF
64 and LOI results can be found in (Table 2).

65

66 Determination of basalt specific surface area using N₂-adsorption BET analysis

67 N₂ adsorption surface area determination was determined at Micromeritics.

68 Prior to BET analysis, samples are sieved to > 6 mm, to allow the sample to fit into the 3 cc sampling
69 bulb. A representative sample is produced using a spinning riffler, and this sample is placed into the
70 sample bulb and weighed on a 4-point balance.

71 The sample bulb is then placed on the NOVA touch outgas station and outgasses for 2 hours at 150°C
72 at vacuum. The final weight of the sample inside the bulb is then determined. The sample is then
73 placed into the instrument on the analysis port. BET (Brunauer, Emmet, and Teller) surface area is
74 determined by using a five-point calibration using nitrogen gas adsorption [$\text{m}^2 \text{g}^{-1}$], from pressures
75 0.1 to 0.3 P P₀⁻¹, at equidistant pressures. The sample weight is inputted into the instruments program
76 to be incorporated into the surface area calculations.

77 For the sample measured and reported in this study (0.996 m₂ g⁻¹), a value correlation coefficient of
78 0.999993 was determined.

79 **S2. ICP-MS methodology**

80 Prior to analysis, samples were filtered through a 0.2 µm filter to remove colloidal particles and
81 acidified to a concentration of 2% HNO₃. The instrument was calibrated using standard solutions.
82 The base cations used in this paper (Na, Mg, K and Ca) were calibrated between 10-30 ppm.

83 Once the samples were prepared for analysis, the concentrations of base cations, as listed above, were
84 determined using Inductively Coupled Plasma-Mass Spectrometry (ICP-MS) on a Thermo-Fisher
85 iCAP-Q at the University of Nottingham. Samples are introduced from an autosampler (Cetac ASX-
86 520) at a flow rate of 1.2 mL min⁻¹, incorporating an ASXpress™ rapid uptake module through a
87 perfluoroalkoxy (PFA) Microflow PFA-ST nebuliser (Thermo Fisher Scientific, Bremen, Germany).
88 Sample processing is undertaken using Qtegra™ software (Thermo-Fisher Scientific) utilizing
89 external cross-calibration between pulse-counting and analogue detector modes when required. The
90 instrument is run using a collision cell charged with He gas and kinetic energy discrimination (KED)
91 to remove polyatomic interferences. Peak dwell times are 100 mS for most elements with 150 scans
92 per sample.

93 Internal standards, used to correct for instrumental drift, are introduced to the sample stream on a
94 separate line (equal flow rate) via the ASXpress unit or are added directly to calibration standards
95 and samples and introduced on a single line. Internal standards typically include combinations of Sc
96 (10 µg L⁻¹), Ge (10 µg L⁻¹), Rh (5 µg L⁻¹) and Ir (5 µg L⁻¹). The matrices used for internal standards,
97 calibration standards and sample diluents is 2% Primar grade HNO₃ (Fisher Scientific, UK) with 4%
98 methanol (to enhance ionization of some elements).

99 External major and minor element calibration standards are used to calibrate the instrument. A
100 bespoke external multi-element calibration solution (PlasmaCAL, SCP Science, France) is used for
101 calibrating Ca, Mg, Na and K at a range of 0-30 mg L⁻¹.

102 Each sample is ran three times, and then a mean concentration from each measurement is determined.
103 This mean concentration is then corrected for minor deviations from the calibration standards and to
104 correct for instrument drift (using the internal standards).

105 **S3. IC methodology**

106 1 mL of non-acidified, filtered and diluted sample were analysed by ion chromatography (Thermo
107 Scientific Dionex™ ICS-1100 Ion Chromatography System). A range of Standard concentration with 0 -
108 20 µg mL⁻¹ was prepared by Instrument check Standard 6 for ion Chromatography, SPEX Certi Prep
109 (Fisher Scientific). F⁻, Cl⁻, N-NO₃⁻, P-PO₄⁻³, S-SO₄⁻² were quantified.

110 **S4. Soil analysis protocol**

111 Most soil analyses were carried out by the United Kingdom Accreditation Service (UKAS) testes and
112 ISO accredited (ISO/IEC 17025:2017) lab NRM - part of Cawood Ltd. Soil pH and bulk density was
113 determined by UNDO.

114 **Organic and Inorganic Carbon**

115 A portion of the dried and ground soil sample is acidified with orthophosphoric acid and sparged at
116 150°C. The gas mixture containing carbon dioxide from the carbonates present in the sample is led
117 by carrier gas to the IR detector. This determines the amount of inorganic carbon present in the
118 sample. The organic carbon (OC) is the difference between the total and the inorganic carbon (TOC =
119 TC – TIC).

120 **Soil CEC / Exchangeable cation content**

121 NRM uses the MAFF RB427 listed Standard Method for Temperate Regions for measuring cation
122 exchange capacities.

123 A small sample of soil is washed with ammonium acetate. Ammonium (NH₄⁺) ions displace all other
124 nutrient cations in the soil into solution and the fraction of each cation in solution is measured and
125 reported in milliequivalents per 100 grams (meq 100 g⁻¹). The soil is then washed with methanol, and
126 again with potassium chloride. The K⁺ ions displace the NH₄⁺ ions into solution, which are then
127 measured to determine the total cation exchange capacity (again reported in meq 100 g⁻¹). The ion
128 concentrations are measured using ICP-OES.

129 **Soil textural classification**

130 The soil sample is suspended in water and passed through a flow cell. The flow cell is positioned in
131 the path of a laser beam and the particles of soil passing through the cell causes the laser light to be
132 diffracted. The amount of light that is diffracted is dependent upon the size of the particle in its path.
133 Small particles cause greater diffraction than large particles. By measuring the diffraction pattern of
134 the laser beam it is possible to predict the size and relative population of particles in the sample. The
135 Laser Diffraction was carried out using a Malvern Mastersizer.

136 Soil bulk density

137 Bulk density was determined in the soil pits where rhizons were installed, using metal rings 5 cm in
138 height and 5 cm in diameter. The rings were inserted horizontally down the pit wall with the
139 installation depth of the rhizons as the middle point of the rings (i.e. the rings were inserted from 2.5
140 - 7.5 cm and 7.5 - 12.5 cm, for the 5 and 10 cm installation depths, respectively). Bulk density was
141 also determined in 30 cm depth (27.5 - 32.5 cm). Following sampling the rings were weighed and
142 dried for 24 hours before the dry mass was determined from the weight of the dry rings including soil
143 minus the weight of the sample rings. Bulk density was calculated as:

144 Bulk density (BD) = $\frac{W_d}{V} g cm^{-3}$

145 W_d = dry mass of soil in g

146 V = volume of soil in cm^3 ~ volume of the sampling ring = $\pi r^2 h$

147 r = radius, and h = height of sampling ring

148 Soil pH

149 Soil pH was determined on a subsample of the homogenized soil sample collected down to 30 cms.
150 The soil samples were analysed in-house for pH and electrical conductivity (using a handheld
151 multimeter probe calibrated against NIST calibration standards) following ISO standard methods ISO
152 10390:2021 and ISO 11265:1994 respectively. Soil pH was measured in water at a ratio of 1:2.5.

153

154 **Table S1.** Whole-rock elemental chemistry, as determined from X-ray fluorescence analysis.

| Oxide | Wt.% |
|--------------------------------|--------|
| Al ₂ O ₃ | 13.53 |
| BaO | 0.04 |
| CaO | 8.62 |
| Cr ₂ O ₃ | 0.01 |
| Fe ₂ O ₃ | 13.73 |
| K ₂ O | 1.11 |
| MgO | 5.98 |
| MnO | 0.18 |
| Na ₂ O | 2.59 |
| P ₂ O ₅ | 0.29 |
| SO ₃ | 0.34 |
| SiO ₂ | 50.41 |
| SrO | 0.06 |
| TiO ₂ | 2.32 |
| XRF total | 100.75 |

155

156

157 **Table S2.** Tukey HSD test results for soil pH for each soil sampling event, where treatment is
 158 compared to the control. Significant values ($p > 0.05$) are emboldened.

159

| Sampling Date | Treatment, t ha ⁻¹ | Mean difference relative to the Control (tCO ₂ ha ⁻¹) | p-value |
|---------------|-------------------------------|--|---------------|
| 19/09/2022 | 23 | -0.108 | 0.2549 |
| | 78 | 0.004 | 0.9999 |
| | 126 | 0.04 | 0.8897 |
| 23/01/2023 | 23 | 0.034 | 0.1414 |
| | 78 | 0.072 | 0.0009 |
| | 126 | 0.248 | 0.0000 |
| 18/04/2023 | 23 | 0.082 | 0.7635 |
| | 78 | 0.134 | 0.4069 |
| | 126 | 0.278 | 0.0204 |
| 11/07/2023 | 23 | 0.154 | 0.2265 |
| | 78 | 0.232 | 0.0365 |
| | 126 | 0.22 | 0.0495 |
| 14/01/2025 | 23 | 0.004 | 1.0000 |
| | 78 | 0.188 | 0.1723 |
| | 126 | 0.054 | 0.9226 |

160

161

162 **Table S3.** Tukey HSD test results for inferred potential carbon dioxide removal (inferred pCDR)
163 from exchangeable cations for each sampling event. Mean differences are calculated for each soil
164 sampling event, where treatment is compared to the control after the baseline results were subtracted.
165 Significant values ($p > 0.05$) are emboldened.

| Sampling Date | Treatment | Mean Difference Relative to the Control (tCO ₂ ha ⁻¹) | p-value |
|-------------------|-----------|--|---------------|
| 23/01/2023 | 23 | -3.4546 | 0.1067 |
| | 78 | -0.4191 | 0.9912 |
| | 126 | 0.3936 | 0.9927 |
| 18/04/2023 | 23 | -2.9626 | 0.8483 |
| | 78 | 1.5414 | 0.9739 |
| | 126 | -0.3826 | 0.9996 |
| 11/07/2023 | 23 | 5.2119 | 0.5548 |
| | 78 | 4.2899 | 0.6945 |
| | 126 | 5.722 | 0.4794 |
| 14/01/2025 | 23 | -4.9741 | 0.0162 |
| | 78 | -0.9438 | 0.9135 |
| | 126 | -3.7752 | 0.0808 |

166

167

168

169

170

171

172

173

174

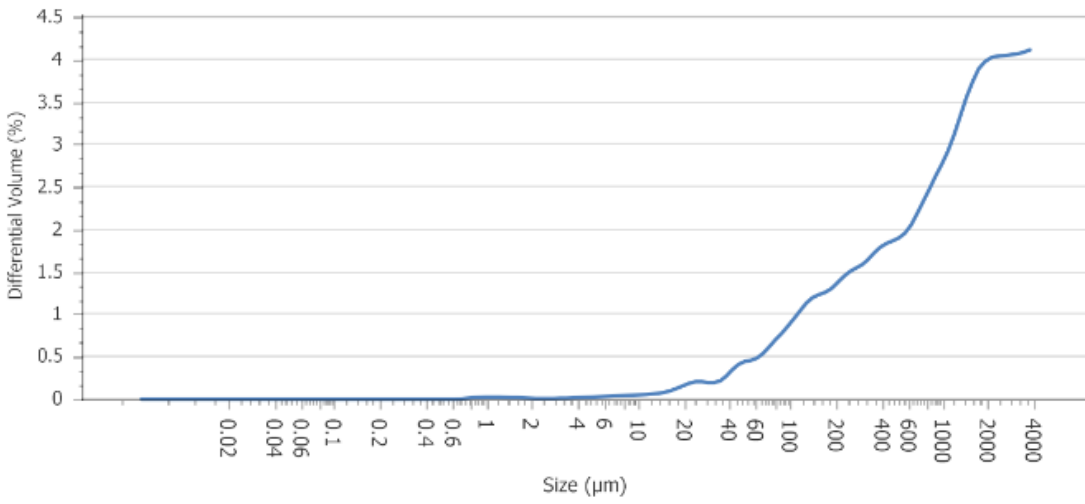
175

176

177

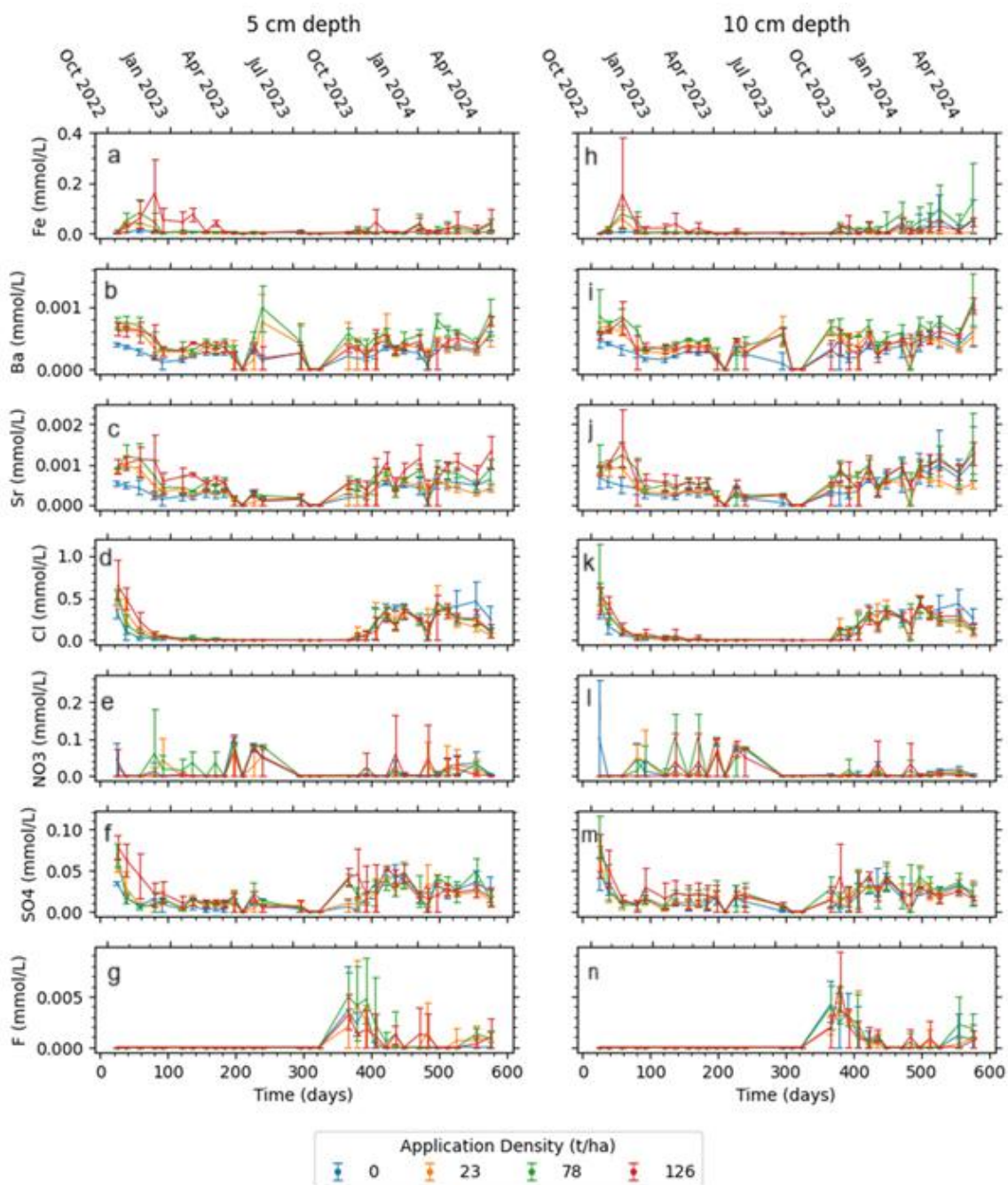
178 **Figure S1.** Particle Size distribution, as determined using laser particle size analysis

179



180

181

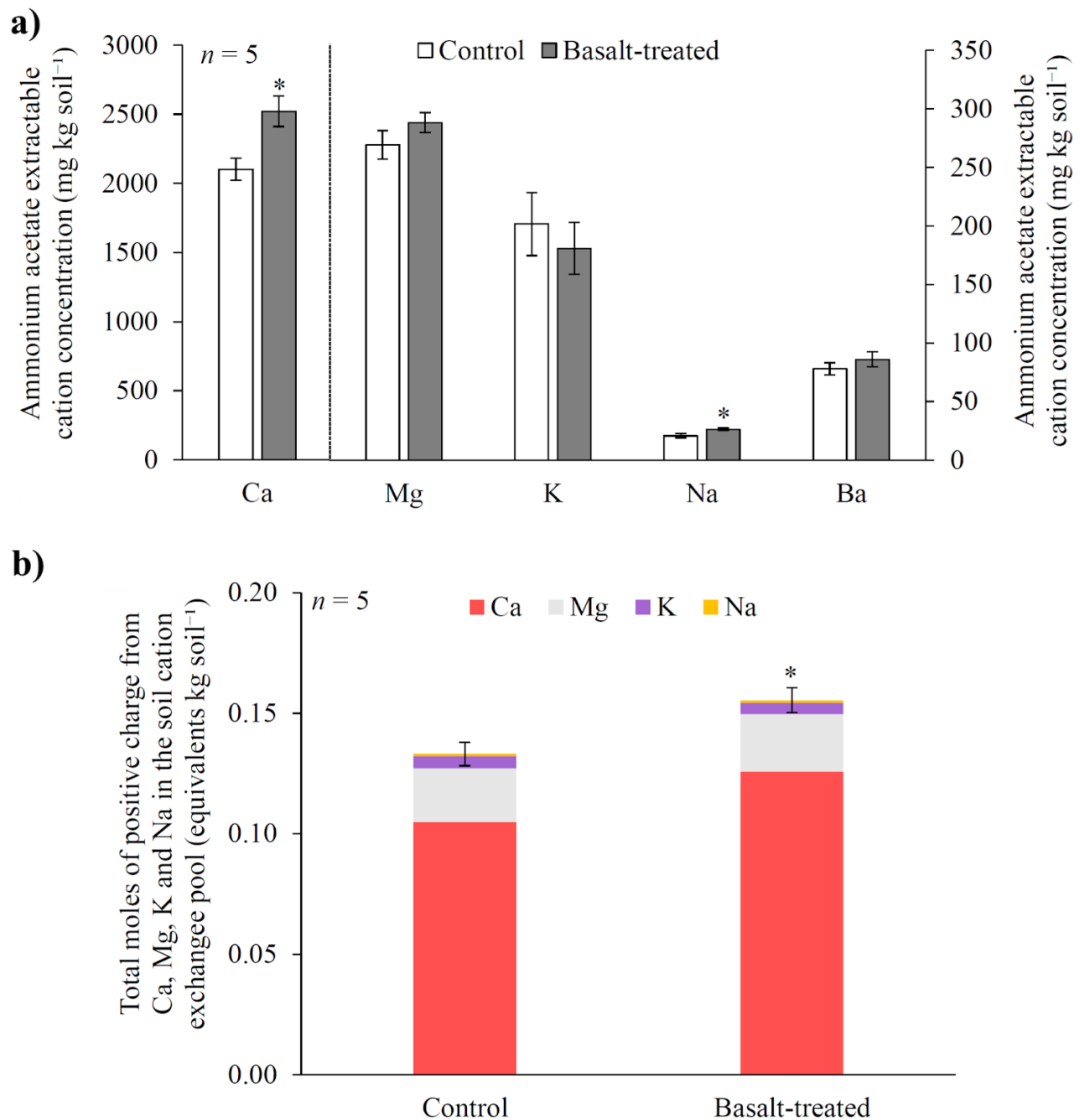


183

184 **Figure S2.** Porewater chemistry throughout the experimental duration at 5 cm depth (a-g) and
 185 10 cm depth (h-m). Points represent mean values, and error bars represent min and max values (n = 3) for
 186 each sampling event.

187

188



189

190 **Figure S3** - Statistically significant differences in sodium and calcium on exchangeable sites (a) and
 191 overall inferred carbon dioxide removal potential (inferred pCDR) (b) observed between control and
 192 126 t ha⁻¹ treatment after (July 2023). Data provided by Weathering Industries Ltd.

193 **References:**

194 Skov, K., Wardman, J., Healey, M., McBride, A., Bierowiec, T., Cooper, J., et al. (2024). Initial
 195 agronomic benefits of enhanced weathering using basalt: A study of spring oat in a temperate
 196 climate. *PLoS One* 19, e0295031-. Available at: <https://doi.org/10.1371/journal.pone.0295031>

197

198

199

200

201